Research Square

Preprints are preliminary reports that have not undergone peer review.
They should not be considered conclusive, used to inform clinical practice,
or referenced by the media as validated information.

Second-Harmonic Generation Through Backward Raman Scattering in Magnetized Plasmas Driven by Circularly Polarized Intense Lasers

A. A. Molavi Choobini

aa.molavich@ut.ac.ir

University of Tehran

S. S. Ghaffari-Oskooei

Alzahra University

Article

Keywords: Backward Raman scattering, Self-modulation, Instability, Magnetized plasma, tapered channel, Interaction of laser and plasma

Posted Date: October 9th, 2026

DOI: https://doi.org/10.21203/rs.3.rs-11012029/v1

License: This work is licensed under a Creative Commons Attribution 4.0 International License.
Read Full License

Additional Declarations: No competing interests reported.

Second-Harmonic Generation Through Backward Raman Scattering in Magnetized Plasmas Driven by Circularly Polarized Intense Lasers

A. A. Molavi Choobini[1*], S. S. Ghaffari-Oskooei[2]

[1]Quantum Matter Lab, Department of Physics, College of Science, University of Tehran, Tehran 14399-55961, Iran,

[2]Department of Atomic and Molecular Physics, Faculty of Physics, Alzahra University, Tehran, Iran.

Abstract:

The nonlinear dynamics of backward Raman scattering (BRS) in a magnetized plasma channel driven by an intense circularly polarized laser pulse are investigated through a combined analytical and numerical approach, with emphasis on the emergence and controllability of a secondary spectral peak. The analysis is performed in the relativistic laser–plasma interaction regime under experimentally relevant plasma densities and axial magnetic-field strengths. A fluid-based theoretical framework is developed to describe the nonlinear cascade linking primary BRS-driven plasma wave amplification, oscillating two-stream instability (OTSI), nonlinear current generation within a self-formed ponderomotive channel, and radiation of the secondary electromagnetic mode. Systematic parameter studies reveal a strong sensitivity of the entire cascade to the relative handedness of laser polarization and axial magnetic field direction, as well as to cyclotron resonance strength. Resonant right-handed circular polarization significantly enhances ponderomotive expulsion, channel depth, BRS and OTSI growth rates, nonlinear current density, and the amplitude of the secondary harmonic, whereas non-resonant left-handed polarization effectively suppresses these processes. Fully kinetic particle-in-cell simulations using EPOCH, together with macroscopic finite-element modelling in COMSOL Multiphysics, corroborate the polarization- and magnetization-dependent wake modulation and channelling efficiency across a wide range of laser wavelengths, pulse durations, and plasma densities. The temporal evolution and saturation of OTSI, resilience to density inhomogeneities, and wavenumber-resolved resonance tuning illustrate axial magnetization as a flexible control mechanism for adjusting the intensity, spectral position, bandwidth, and stability of multi-peak Raman spectra. These findings demonstrate that cyclotron resonance and polarization control are effective methods for manipulating nonlinear Raman emission in high-intensity laser–magnetized plasma interactions, offering predictive insights for forthcoming kinetic simulations and experimental implementations.

PACS: 52.38.-r, 52.35.Mw, 52.65.Rr

Keywords: Backward Raman scattering, Self-modulation, Instability, Magnetized plasma, tapered channel, Interaction of laser and plasma.

*Corresponding author: E-mail address: aa.molavich@ut.ac.ir

I. Introduction

Second-harmonic generation (SHG) is one of the most fundamental nonlinear optical processes, in which two photons of frequency ω are coherently converted into a single photon of frequency 2ω. Since its first observation in crystalline quartz, SHG has become a powerful diagnostic and frequency-conversion technique in laser physics, ultrafast optics, and spectroscopy. It provides a

route to extend laser sources into new spectral ranges, generate ultrashort pulses at harmonic wavelengths, and probe material properties with symmetry-selective sensitivity [1–5].

Traditionally, SHG is realized in bulk nonlinear crystals such as lithium niobate ($LiNbO_3$), potassium dihydrogen phosphate (KDP), or beta barium borate (BBO). These media offer high conversion efficiency under proper phase-matching conditions but suffer from limitations such as optical damage thresholds, finite transparency ranges, and crystal birefringence [6, 7]. Surface- and interface-based SHG, including plasmonic nanostructures, alleviate some of these limitations through local field enhancement, although they are generally narrowband and sensitive to fabrication imperfections. More recently, two-dimensional materials and metamaterials have emerged as compact and tunable SHG platforms, albeit with lower conversion efficiencies than bulk crystals [8, 9]. Plasmas generated by high-intensity lasers provide an attractive alternative because they are immune to optical damage and sustain extremely high electromagnetic fields. Unlike bound-electron nonlinearities in solids, plasma SHG originates from collective free-electron dynamics involving ponderomotive forces, relativistic effects, plasma-wave excitation, and nonlinear wave coupling [10–12].

In this respect, Oks and team [13] observed SHG in femtosecond laser-driven cluster plasmas, where rapid laser-induced electron heating generated nonlinear plasma oscillations and anharmonic currents. Ahmed et al. [14] and Gupta et al. [15] showed that relativistic self-focusing of q-Gaussian and Laguerre-Gaussian beams enhances plasma-wave excitation and SHG in underdense plasmas. Walia [16] demonstrated that density gradients produced by non-uniform laser heating excite plasma waves, whose nonlinear interaction with the incident laser enhances SHG, whereas Sharma and co-workers [17] reported resonant SHG arising from self-focusing and wave coupling near the critical incidence angle in magnetized plasmas. Ganeev [18] reviewed several harmonic-enhancement mechanisms, including resonant excitation, quasi-phase matching, two-color pumping, and nanoparticle-assisted plasmas. Beier and Dollar [19] investigated high-order harmonic generation from relativistic plasma mirrors driven by orthogonally polarized two-color laser fields, while Mathijssen and team [20] demonstrated that sub-cycle field shaping modifies electron trajectories and controls harmonic emission. Garriga Francis et al. [21, 22] and Lim Pac Chong et al. [23] developed THz-field-induced second-harmonic generation (TFISH), in which nonlinear THz-driven currents generate SHG in plasma filaments. Huang et al. [24] experimentally demonstrated spin-to-orbital angular momentum (OAM) conversion during SHG in underdense plasmas, whereas Shing Yiu Fu and colleagues [25] investigated the temporal and polarization dynamics responsible for enhanced SHG in laser-induced air plasmas. Kim and team [26] demonstrated continuous high-order harmonic generation from a liquid-sheet plasma mirror, providing a damage-free platform for high-repetition-rate harmonic generation. These studies indicate that plasma harmonic generation can be achieved through different nonlinear mechanisms, including laser-induced electron heating, plasma-wave excitation, self-focusing, nonlinear current generation, and wave-wave coupling. However, the coupled effects of BRS, oscillating two-stream instability (OTSI), and externally applied magnetic fields on SHG have not yet been systematically investigated. This work addresses this gap by developing a unified analytical macroscopic cold-fluid and kinetic framework for magnetized underdense plasmas.

A numerical and analytical fluid-based framework for understanding and controlling nonlinear laser–plasma interactions in cold magnetized plasmas is developed. The proposed framework self-consistently couples cyclotron-resonant ponderomotive channeling, backward Raman scattering (BRS), oscillating two-stream instability (OTSI), and nonlinear axial-current-driven second-harmonic generation (SHG) into a unified description of nonlinear Raman spectra. Unlike previous studies, which primarily considered unmagnetized plasmas or isolated nonlinear processes, the present model incorporates arbitrary axial magnetization and consistently describes the polarization-dependent ponderomotive force, plasma density perturbation, instability growth, nonlinear current generation, and second-harmonic emission within a single analytical formulation. Cyclotron resonance and laser polarization handedness emerge as experimentally accessible control parameters for tuning the nonlinear response of the plasma. The enhancement mechanism follows a hierarchical sequence in which BRS first amplifies a Langmuir wave, the amplified plasma wave subsequently drives OTSI, OTSI strengthens the plasma density modulation and nonlinear current, and the nonlinear current acts as the source term for SHG. The externally applied magnetic field regulates both BRS and OTSI through electron cyclotron resonance, providing a direct means of controlling harmonic generation. Macroscopic finite-element simulations using COMSOL Multiphysics are performed together with the analytical cold-fluid model to investigate plasma-channel formation, wake modulation, and magnetization-dependent instability development over a range of laser wavelengths, pulse durations, and plasma densities. Fully kinetic PIC simulations using the EPOCH code provide a complementary description by resolving electron phase-space dynamics beyond the fluid approximation, including particle trapping, velocity-space bunching, nonlinear current filamentation, and OTSI. The agreement between the analytical model, COMSOL simulations, and PIC calculations demonstrates the robustness of the proposed mechanism across fluid, macroscopic, and kinetic descriptions. The external magnetic fields considered in this work are motivated by recent laser-driven capacitor-coil experiments demonstrating kilo-tesla magnetic-field generation [27,28]. Besides representing experimentally accessible magnetized plasmas, these fields govern electron cyclotron resonance, thereby controlling the polarization dependence of BRS, OTSI growth, nonlinear current generation, and SHG. The paper is organized as follows. Section II presents the theoretical formulation for laser propagation in magnetized plasma channels. Section III describes the analytical and numerical methods. Section IV presents and discusses the results. Finally, Section V summarizes the main conclusions.

II. General Mechanism

Consider a circularly polarized laser pulse propagating through a magnetized plasma channel immersed in a static magnetic field $\vec{B} = B_0\hat{e}_z$ (Fig. 1). The electric field of the laser pulse is given by:

$$\vec{E}_L(\vec{r},t) = \frac{1}{2}E_L\left(\hat{e}_x + i\sigma\hat{e}_y\right)e^{-i\omega_0 t + ik_0 z} + c.c. \tag{1}$$

where E_L, ω_0, and k_0 denote the amplitude, frequency, and wavevector of the laser, respectively. The parameter $\sigma = \pm 1$ indicates the handedness of the right or left circular polarizations. During

the propagation of the circularly polarized laser pulse in the plasma, the electron quiver velocity is expressed as:

$$\vec{v}_0 = -i\frac{e}{m_e(\omega_0-\sigma\omega_c+i\nu_c)}\vec{E}_L \tag{2}$$

Here, ν_c is the collisional frequency, $\omega_c = eB_0/m_e c$ represents the electron cyclotron frequency, and the m_e and c are the electron mass and the speed of light, respectively. The laser's electric field induces a ponderomotive force on the electrons, described as:

$$\vec{F}_{pond} = \frac{m_e}{2}\left(1-\frac{\sigma\omega_c}{\omega_0}\right)\vec{\nabla}v_0^2 \tag{3}$$

The ponderomotive force can also be written as $\vec{F}_{pond} = e\vec{\nabla}\phi_{pond}$, where the ponderomotive potential is given by:

$$\phi_{pond} = \frac{e|E_L|^2}{2m_e[(\omega_0-\sigma\omega_c)^2+\nu_c^2]}\left(1-\frac{\sigma\omega_c}{\omega_0}\right) \tag{4}$$

The ponderomotive force perturbs plasma density. The perturbation in plasma density, denoted by n_s, is related to the ponderomotive force by the equation:

$$\left(\frac{\partial^2}{\partial t^2}+\nu_c\frac{\partial}{\partial t}+\omega_p^2\right)\frac{n_s}{n_0} = -\frac{e}{m_e}\nabla^2\phi_{pond} \tag{5}$$

Assuming a Gaussian laser profile, $E_L^2 = E_0^2\exp(-\frac{r^2}{r_0^2})$, the density perturbation is derived as:

$$n_s = -2n_0(1-\frac{r^2}{r_0^2})\left(1-\frac{\sigma\omega_c}{\omega_0}\right)\frac{v_0^2}{c^2} \tag{6}$$

This result implies that when $r_0 \cong c/\omega_p$, the density perturbation can be approximated as $\frac{n_s}{n_0} = -\frac{v_0^2}{c^2}\left(1-\frac{\sigma\omega_c}{\omega_0}\right)$. The propagation of a laser pulse in a plasma medium and the resulting perturbation of plasma density led to various instabilities. One notable is BRC, a parametric instability arising from the interaction between the laser pulse and plasma waves. Experimental studies reveal that the frequency spectrum of this instability comprises two red-shifted peaks at $\omega_0-\omega$ and $2\omega_0-2\omega$, where ω denotes the plasma wave frequency. The electric field corresponding to the first red-shifted peak, also known as the Stokes sideband, is expressed as:

$$\vec{E}_1 = \frac{1}{2}E_1\left(\hat{e}_x+i\sigma\hat{e}_y\right)e^{-i\omega_1 t-ik_1 z}+c.c. \tag{7}$$

Here, $\omega_1 = \omega_0-\omega$ and $k_1 = k_0-\mathrm{k}$ represent the frequency and wavevector of the Stokes sideband in Raman backscattering, where k is the wavevector of the plasma wave. For the case of magnetized plasma, as considered in this study, the growth rate associated with the first red-shifted peak is derived analytically in Ref. [1] using a mathematical analysis based on the fluid theory of magnetized plasmas. The growth rate is given by:

$$\Gamma = \frac{eE_0\sqrt{\omega_0\omega_{pe}}}{2m_e\omega_0 c(1-\frac{\sigma\omega_c}{\omega_0})} \tag{8}$$

where ω_{pe} is the electron plasma frequency. Plasma waves experience amplification during Raman backward scattering [29, 30], making them susceptible to OTSI. These amplified plasma waves also contribute to the formation of a plasma channel. The propagation of Raman backscattered wave through this plasma channel results in a nonlinear current density, which generates the second-harmonic component at ω_2. To mathematically analyze the second-harmonic generation driven by the nonlinear current in Raman backscattering, we begin with the OTSI, which arises in the presence of large-amplitude plasma waves. These waves, amplified during Raman backscattering, perturb the electric potential associated with the space charge. The perturbed electric potential is expressed as:

$$\phi'(\vec{r},t) = \frac{1}{2}\phi' e^{-i(\omega' t - k' z)} + c.c. \tag{9}$$

where $\omega'$and k'denote the frequency and wavevector of the low-frequency perturbation (modulation), respectively. This process generates two sidebands:

$$\phi_+(\vec{r},t) = \frac{1}{2}\phi_+ e^{-i(\omega_+ t - k_+ z)} + c.c. \tag{10}$$

$$\phi_-(\vec{r},t) = \frac{1}{2}\phi_- e^{-i(\omega_- t - k_- z)} + c.c. \tag{11}$$

the corresponding upper and lower sidebands satisfy the frequency and wavevector matching relations $\omega_\pm = \omega \pm \omega'$and $k_\pm = k \pm k'$, respectively. The ponderomotive force arising from the electric fields associated with $\phi_\pm$ is given by [2]:

$$\mathbf{F}'_{pond} = \frac{e}{2}\vec{\nabla}\left(\frac{k_+\phi_+ v^*}{\omega_+} + \frac{k_-\phi_- v}{\omega_-}\right) \tag{12}$$

Consequently, the ponderomotive potential can be expressed as

$$\phi'_{pond} = \frac{e}{2}\left(\frac{k_+\phi_+ v^*}{\omega_+} + \frac{k_-\phi_- v}{\omega_-}\right) \tag{13}$$

The sideband plasma waves perturb the electron and ion densities. To evaluate these perturbations, n'_e and n'_i, the analysis begins with the Vlasov equation:

$$\left(\frac{\partial}{\partial t} + \mathbf{v}\cdot\nabla_x - \frac{e\mathbf{E} + mc^2\nabla\phi'_{pond}}{m_e}\cdot\nabla_v\right) f_e = 0 \tag{14}$$

where f_e is the electron distribution function. By applying the perturbative expansion $f_e = f_0 + \delta f_e$and $n'_e = \int \delta f_e \, d\mathbf{v}$, the electron density perturbation is derived as follows:

$$n'_e = \frac{k'^2}{4\pi e}\chi_e\left(\phi' + \phi'_{pond}\right) \tag{15}$$

where $\chi_e = -\frac{\omega_{pe}^2}{\omega'^2}$ is the electron susceptibility. Similarly, the ion density perturbation satisfies:

$$n'_i = \frac{k'^2}{4\pi e}\chi_i\phi' \tag{16}$$

where $\chi_i = \frac{\omega_{pi}^2}{k'^2 C_{si}^2}$ is ion susceptibility, C_{si} is the ion-acoustic speed, and ω_{pi} is the ion-plasma frequency. Since the formation of the density-modulated plasma channel is governed by the growth of plasma density perturbations, the growth rate of the OTSI must first be evaluated. The OTSI growth rate by combining the linearized electron and ion density perturbations with the nonlinear sideband coupling induced by the ponderomotive interaction between the pump wave and the upper and lower sidebands, and the corresponding dispersion relation expresses as:

$$\Gamma_{\mathrm{OTSI}} = \frac{\omega_{pe}|v_0|^2}{v_{th_i}^2}\left(1+\frac{\omega_{pi}^2}{k^2 C_{si}^2}\right)^{-1} = \frac{\omega_{pe}}{v_{th_i}^2}\frac{e^2 E_L^2}{m_e^2[(\omega_0-\sigma\omega_c)^2+\nu_c^2]}\left(1+\frac{\omega_{pi}^2}{k^2 C_{si}^2}\right)^{-1} \tag{17}$$

where v_0 is the magnetized electron quiver velocity given by Eq. (2). Here, v_{th_i} denotes the effective ion-thermal velocity associated with the ion-acoustic response retained in the coupled plasma-wave model, rather than arising from a thermal-pressure correction to the electron momentum equation. Equation (17) should therefore be regarded as the magnetized extension of the standard OTSI growth-rate expression. In the unmagnetized limit ($\omega_c \to 0$) and in the collisionless limit ($\nu_c \to 0$), the magnetized quiver velocity reduces to its conventional form reported by Liu and Tripathi [31]. Equation (17) describes the growth rate of the OTSI driven by the finite-amplitude plasma wave established through the preceding BRS process. The resulting density-modulated plasma channel enhances the nonlinear current density responsible for the generation of the second harmonic. The amplitude of the corresponding electric field E_2 is evaluated through the solution of Maxwell's equations. Unlike the classical laser-driven OTSI typically investigated near the critical density, the instability considered here is triggered by the large-amplitude Langmuir wave generated through BRS in an underdense magnetized plasma. Accordingly, the density range $0.01n_c \leq n_e \leq 0.1n_c$ is intentionally selected to preserve laser transparency while maximizing BRS amplification. Similar plasma-wave-driven OTSI has previously been reported for laser wakefield- and plasma beat-wave-generated Langmuir waves, supporting the physical mechanism adopted here [32, 33].

To evaluate E_2, two perturbative contributions must be included in the analysis. Accordingly, the perturbed electron velocity consists of two components, $v_1$and v_2. The first part ($\vec{v}_1$) is the velocity of electrons accelerated in the electric field of $\vec{E}_1$:

$$\vec{v}_1 = -i\frac{e}{m_e(\omega_1-\sigma\omega_c)}\vec{E}_1 \tag{18}$$

The second part ($\vec{v}_2$) is expressed as:

$$\vec{v}_2 = -i\frac{e}{m_e(\omega_2-\sigma\omega_c)}\vec{E}_2 - i\frac{1}{2(\omega_1-\sigma\omega_c)}\vec{\nabla}v_1^2 \tag{19}$$

where $\vec{E}_2$ is the electric field is associated with the second harmonic. The second term in Eq. (19) indicates the contribution of the ponderomotive force to the generation of the second harmonic. If the initial plasma density in the channel is expressed as $n_i = n_0 + n_s$, the perturbation in the plasma density will be given by $n_1 = \frac{\vec{v}_1.\vec{\nabla}n_i}{i\omega_1}$. This density modulation contributes directly to the

nonlinear current density J_{NL}, particularly through the density-dependent term proportional to $n_s \nabla v_1^2$, which acts as the source term for SHG. Therefore, the current density is given by:

$$\mathbf{J} = i\frac{e^2 n_0}{m_e(\omega_2 - \sigma\omega_c)}\mathbf{E}_2 + i\frac{\mathbf{v}_1 \cdot \nabla n_i(r,z)}{\omega_2}\mathbf{v}_1 + i\frac{n_s e}{4(\omega_2 - \sigma\omega_c)}\nabla \mathbf{v}_1^2 \tag{20}$$

The magnetic field of the second harmonic satisfies Maxwell's equation

$$-\nabla^2 \mathbf{B}_2 + \frac{1}{c^2}\frac{\partial^2 \mathbf{B}_2}{\partial t^2} = \frac{4\pi}{c}\nabla \times \mathbf{J} \tag{21}$$

By substituting the current density from Eq. (20) into Eq. (21) and assuming a dependence on z of the form $\exp[i(k_{2z}z - \omega_2 t)]$, the wave equation for the second-harmonic magnetic field becomes

$$\left(\frac{\partial^2}{\partial x^2} + k_{2x}^2\right) B_{2y} = \frac{2\pi e}{c(\omega_2 - \sigma\omega_c)}(k_{2z} - 2k_0)\, v_1^2 \frac{\partial n_s}{\partial x} \tag{22}$$

and

$$\left(\frac{\partial^2}{\partial x^2} + k_{2x}^2\right) B_{2x} = 0 \tag{23}$$

Here, the dispersion relation for the second harmonic is expressed as:

$$\omega_2^2 = c^2(k_{2x}^2 + k_{2z}^2) + \frac{\omega_{pe}^2}{1 - \sigma\omega_c/\omega_2} \tag{24}$$

Therefore, the SHG enhancement mechanism considered in the present work follows the sequence

$$(\omega_0, k_0) \rightarrow \text{BRS} \rightarrow \text{OTSI} \rightarrow n_s \rightarrow J_{NL} \rightarrow (\omega_2, 2k_0).$$

Specifically, the incident circularly polarized pump laser excites BRS, which generates and amplifies an electron plasma (Langmuir) wave. The amplified plasma wave subsequently triggers OTSI, leading to density modulation (n_s) and enhanced nonlinear current density (J_{NL}). The nonlinear current acts as the direct source of SHG, whereas BRS and OTSI enhance SHG indirectly by strengthening the plasma-wave amplitude and nonlinear current. Solving Eqs. (22) and (23) yields the second-harmonic electromagnetic field and its corresponding intensity.

III. Results & Discussion

To validate the analytical framework delineated in the preceding section and to examine the nonlinear dynamics of BRS in a magnetized plasma channel driven by a circularly polarized laser pulse, extensive numerical simulations were conducted utilizing two complementary methodologies: finite-element method (FEM) simulations with COMSOL Multiphysics and fully kinetic PIC simulations employing the EPOCH code. The Wave Optics Module of COMSOL Multiphysics coupled with a magnetized cold-fluid plasma dielectric model was employed to simulate the macroscopic electromagnetic response of the plasma. This approach describes electromagnetic wave propagation, ponderomotive channel formation, plasma density perturbations, and the influence of an externally applied static magnetic field on wave dispersion, whereas microscopic kinetic effects are resolved independently using fully kinetic PIC

simulations. The analytical model is developed within the non-relativistic cold-fluid approximation. For the laser parameters considered in this work ($\lambda = 1\ \mu$m, $I = 10^{18} - 10^{20}$ W/m^2), the normalized vector potential is $a_0 = 8.5 \times 10^{-4} - 8.5 \times 10^{-2}$, remaining well below the relativistic threshold ($a_0 < 1$); therefore, relativistic corrections are neglected. A Gaussian circularly polarized laser pulse with normalized amplitude $a_0$was injected into a preformed plasma channel with electron density $n_e \approx 0.01 - 0.1\, n_c$(where $n_c$is the critical density) immersed in an axial magnetic field of strength $B_0 \approx 10 - 100$ T, corresponding to $\omega_c/\omega \approx 0.1 - 0.5$ [34–37]. The simulations employed a two-dimensional axisymmetric geometry to resolve the radial plasma-density profile and ponderomotive channelling, enabling detailed analysis of BRS, plasma-wave amplification, and the onset of OTSI. In addition, fully kinetic PIC simulations were performed using the EPOCH code (development branch based on version 4.19-devel, circa mid-2025) [38], which self-consistently solves the relativistic Vlasov-Maxwell equations using the particle-in-cell method. These simulations capture kinetic processes beyond the fluid model, including relativistic electron dynamics, particle trapping, nonlinear wave evolution, instability saturation, and higher-order scattered waves. The simulation domain typically extended over $100 - 200\ \lambda$in the propagation direction and $20 - 50\ \lambda$transversely, using $10^3 - 10^4$grid cells in each direction with 50–100 macro-particles per cell per species, ensuring adequate resolution of both the plasma wavelength ($\lambda_p \approx 10 - 20\ \mu$m) and the Debye length. A Gaussian circularly polarized laser pulse with parameters identical to those used in the COMSOL simulations was launched from the left boundary into a uniform or preformed underdense magnetized plasma. A moving-window technique was adopted to follow the laser pulse over extended propagation distances, allowing the nonlinear evolution of BRS, OTSI saturation, particle trapping, and the emergence of the second-harmonic spectral component to be resolved.

The COMSOL simulations in Fig. 2 illustrate the propagation of an intense circularly polarized laser pulse through a magnetized plasma channel at different laser wavelengths, providing insight into ponderomotive channel formation and the onset of nonlinear instabilities. Panel (a) (λ = 1064 nm) exhibits the strongest trailing modulation and filamentary structures. The larger normalized vector potential a_0(for fixed peak intensity) enhances the ponderomotive force, producing deeper plasma-density cavities and stronger plasma-wave excitation. Consequently, the trailing envelope develops irregular structures characteristic of early nonlinear saturation and wave steepening, consistent with the onset of BRS, whose growth rate increases with a_0, favoring amplification of the Stokes sideband at $\omega_s \approx \omega_0 - \omega_{pe}$. As the wavelength decreases from 800 nm (panel b) to 532 nm (panel c) and 400 nm (panel d), the trailing modulation becomes weaker, although the evolution is not strictly monotonic because of the nonlinear laser-plasma interaction. The corresponding reduction in a_0 weakens the ponderomotive force, leading to shallower density perturbations and reduced wake excitation. The laser envelope remains smoother with less transverse filamentation. Lower $a_0$suppresses the convective growth of BRS and delays the onset of OTSI, which requires sufficiently amplified plasma waves to drive nonlinear currents. The external axial magnetic field further stabilizes transverse modes while promoting axial plasma-wave propagation. The transition from strongly modulated propagation at λ = 1064 nm to relatively stable propagation at λ = 400 nm highlights the critical role of $a_0$in controlling Raman-related instabilities in magnetized plasma channels.

Figure 3 illustrates the influence of pulse duration (τ_L) on laser-plasma interaction in a magnetized channel obtained from COMSOL simulations. As the pulse duration increases, the interaction evolves from weakly modulated propagation to a strongly nonlinear regime because of the cumulative action of the ponderomotive force over multiple plasma periods. For the shortest pulse ($\tau_L = 5$ fs, panel a), the laser envelope remains nearly coherent with only weak trailing oscillations. The limited interaction time produces only small density perturbations, restricting plasma-wave excitation and slowing the convective growth of BRS. Increasing the pulse duration to 10 fs (panel b) and 20 fs (panel c) strengthens wake excitation, deepens the density cavity, and enhances plasma-wave amplification, resulting in more pronounced axial modulation and filamentation. The external magnetic field suppresses transverse breakup while promoting axial plasma-wave growth, providing favorable conditions for OTSI. At the longest duration ($\tau_L = 40$ fs, panel d), strong filamentation, turbulent wake structures, and extended oscillations indicate cumulative plasma-wave amplification sufficient for OTSI saturation and particle trapping. These observations agree with the fluid-based growth-rate analysis, which predicts that longer interaction times provide larger gain lengths for both BRS and OTSI while enhancing ponderomotive channel formation. Figure 4 shows the influence of plasma density (n_p) on laser propagation in a magnetized plasma channel obtained from COMSOL simulations. At the lowest density (panel a), the wake exhibits strong filamentation and pronounced oscillations. The low plasma frequency produces a longer plasma wavelength and weaker damping, allowing efficient ponderomotive electron expulsion, deep density cavitation, and strong BRS amplification. The resulting plasma waves readily trigger OTSI and the associated nonlinear currents. As the plasma density increases, the higher ω_{pe} shortens the plasma wavelength and increases wave damping, progressively reducing wake amplitude, filamentation, and plasma-wave amplification. The system approaches the threshold below which sustained BRS and OTSI cannot be maintained, making pronounced Stokes-wave generation increasingly unfavorable. These density-dependent trends are consistent with the analytical model presented in Section II, where the BRS growth rate decreases with increasing ω_{pe} in the underdense regime, while OTSI requires plasma-wave amplitudes above a critical threshold. The external magnetic field modifies the dispersion through cyclotron resonance, although the plasma frequency remains the dominant

The analytically calculated radial ponderomotive force profiles, shown in Fig. 5, illustrate the influence of laser polarization handedness and external magnetic field strength on electron expulsion in a magnetized plasma channel. Right-handed circular polarization produces a substantially stronger radial ponderomotive force than left-handed polarization over the entire range of cyclotron frequencies considered. This asymmetry arises because the rotating laser electric field co-rotates with the electron cyclotron motion (for B_0directed along the propagation axis), enhancing the electron quiver velocity and increasing the effective ponderomotive potential. The larger radial force produces deeper density cavitation and facilitates plasma-channel formation. In contrast, left-handed polarization rotates opposite to the electron gyromotion, reducing the quiver amplitude and yielding a much weaker ponderomotive force, with peak values nearly one order of magnitude smaller for the same ω_c. The influence of the magnetic field becomes increasingly pronounced as $\omega_c$increases from $0.1\omega_0$ to $0.9\omega_0$. Stronger cyclotron resonance enhances electron expulsion for the resonant ($\sigma = +1$) configuration, whereas the non-

resonant ($\sigma = -1$) profiles exhibit only minor changes. At large radial distances, all force profiles approach zero because of the Gaussian laser envelope. The steeper radial gradients obtained under resonant conditions indicate stronger transverse confinement and more efficient self-channeling, providing favorable conditions for plasma-wave excitation and subsequent nonlinear laser-plasma interaction.

The analytical results presented in Fig. 6 illustrate the dependence of plasma channelling and density perturbation on laser polarization and external magnetic field strength. In panel (a), the channelling parameter $r_0\omega_c/c$, which determines the balance between ponderomotive self-focusing and diffraction, increases markedly for right-handed circular polarization, particularly under strong cyclotron resonance. Values exceeding ~ 20indicate efficient relativistic self-channelling over multiple Rayleigh lengths. This behavior results from resonant amplification of the electron quiver motion and the associated enhancement of the ponderomotive force. In contrast, left-handed polarization produces consistently smaller values of $r_0\omega_c/c$, indicating weak channel formation because the laser rotation is opposite to the electron gyromotion. This polarization asymmetry is reflected in the radial density profiles shown in panel (b). Under resonant right-handed polarization, the plasma density exhibits strong on-axis depletion, with n/n_0approaching zero at $r = 0$and recovering rapidly beyond the laser spot size r_0, consistent with the Gaussian-derived density perturbation. Increasing $\omega_c$further enhances density cavitation, producing a broader low-density waveguide that supports long-distance wave propagation and stronger wave coupling. In the non-resonant configuration, the plasma density remains above $n/n_0 > 0.9$, indicating weak electron expulsion and poor channel formation. The difference between the two panels demonstrates that cyclotron resonance governs plasma-channel formation and density modulation. Under resonant conditions, the deeper plasma channel lowers the threshold for BRS and promotes plasma-wave amplification toward OTSI. The amplified plasma waves generate the nonlinear current responsible for SHG, whereas non-resonant configurations suppress these processes and reduce instability growth. The radial plasma-density perturbations obtained from the analytical model and PIC simulations are consistent with the available experimental observations [39].

The analytically calculated parameter-space distribution of the BRS growth rate Γ_{BRS}, shown in Fig. 7, illustrates the combined influence of plasma density (ω_{pe}/ω_0) and external magnetic field strength (ω_c/ω_0) in a magnetized plasma. The growth-rate surface exhibits a broad high-growth region, with peak values exceeding $2.5 \times 10^{13}\ \mathrm{s}^{-1}$along a ridge centered at $\omega_{pe}/\omega_0 \approx 0.2 - 0.4$ and $\omega_c/\omega_0 \approx 0.3 - 0.7$. This ridge corresponds to optimal phase-matching and cyclotron-resonance conditions, where the ponderomotive-driven plasma wave couples efficiently to the backscattered electromagnetic wave while maintaining favorable electron mobility along the propagation direction. For low plasma densities ($\omega_{pe}/\omega_0 \to 0$), the growth rate approaches zero because the plasma response and scattering efficiency become too weak to sustain BRS, consistent with the underdense condition $\omega_{pe} \ll \omega_0$. As ω_{pe}/ω_0approaches unity, Γ_{BRS}decreases rapidly because the plasma approaches the critical-density regime, where group-velocity matching deteriorates and relativistic channel formation becomes less efficient. The magnetic-field dependence is also non-monotonic. Weak magnetic fields ($\omega_c/\omega_0 \to 0$) provide only moderate

growth because of limited electron magnetization, whereas strong magnetic fields suppress the instability through cyclotron-induced dispersion and damping, restricting plasma-wave excitation. The broad high-growth plateau at intermediate values of both parameters identifies the operating regime where amplified plasma waves exceed the OTSI threshold, enabling nonlinear current generation in the self-formed plasma channel and subsequent SHG. The sharp boundaries of this region indicate strong sensitivity to plasma density and magnetic-field strength, showing that modest parameter variations can move the system below the instability threshold and suppress BRS.

The time evolution of the OTSI growth rate, shown in Fig. 8, illustrates its dependence on the normalized wave number (k/k_p) and normalized magnetic field strength during the nonlinear evolution of a magnetized plasma channel. At the earliest time (panel a), the growth-rate distribution is broad, covering a wide range of $k$and B_0. This regime represents the initial linear stage, where plasma waves amplified by BRS perturb the ponderomotive potential but have not yet reached amplitudes sufficient for strong OTSI selectivity. The broad high-growth region is consistent with the fluid model, in which Γ_{OTSI}depends on the plasma-wave amplitude, which remains relatively small at early times. At $t = 10$fs (panel b), the growth-rate distribution becomes structured, with partial suppression at larger $k$and stronger magnetic fields. This behavior indicates the onset of nonlinear feedback associated with particle trapping and wave saturation, which modify the effective plasma susceptibility. The persistence of high Γ_{OTSI}at intermediate wave numbers indicates efficient coupling of the Stokes sideband to resonant plasma-wave modes, supporting nonlinear current generation within the evolving plasma channel. At $t = 50$fs (panel c), the high-growth region contracts toward lower wave numbers and moderate magnetic fields, while Γ_{OTSI}decreases rapidly elsewhere. This localization indicates the transition to the nonlinear saturation stage, where particle trapping in the BRS-amplified plasma wave suppresses further exponential growth. The remaining unstable modes correspond to longer wavelengths that are less susceptible to Landau damping and cyclotron-induced stabilization, allowing coherent wake structures capable of sustaining the nonlinear current responsible for SHG. At $t = 100$fs (panel d), the instability is confined to a narrow band at low $k$and weak-to-moderate magnetic fields, with nearly complete suppression throughout the remaining parameter space. This distribution indicates advanced saturation, where wave breaking, particle detrapping, and pump depletion stabilize the plasma channel against further OTSI growth. The residual low-k instability is attributed to long-lived nonlinear wake structures that continue to support weak harmonic generation.

The analytical dependence of the BRS growth rate on the normalized plasma frequency is presented in Fig. 9 for different laser polarizations and magnetic-field strengths. The results demonstrate that Γ_{BRS} is strongly influenced by both polarization handedness and cyclotron resonance. For right-handed circular polarization, the growth rate increases rapidly with ω_{pe}/ω_0throughout the underdense regime, with the largest values obtained at higher cyclotron frequencies. Under these resonant conditions, cyclotron motion enhances the electron quiver velocity and ponderomotive force, improving phase matching between the pump, plasma wave, and Stokes sideband while maintaining favorable axial wave propagation. As a result, significant BRS growth is sustained over a broad density range. At lower magnetic-field strengths, the growth rate remains substantial but decreases because the cyclotron-resonance enhancement becomes

weaker. In contrast, left-handed circular polarization produces much smaller growth rates over nearly the entire density range because the counter-rotating electron motion suppresses resonance, reducing ponderomotive electron expulsion and plasma-wave excitation. The polarization asymmetry becomes increasingly pronounced as the magnetic field increases, clearly separating the resonant and non-resonant configurations. As ω_{pe}/ω_0approaches unity, the growth rates for all cases converge because the plasma approaches the critical-density regime, where the underdense approximation gradually breaks down and linear absorption becomes dominant.

The analytically calculated radial distribution of the normalized nonlinear current density, $|J_{NL}|$, is presented in Fig. 10. The current is obtained from the laser-driven electron velocity perturbations and the ponderomotive contribution derived in the analytical model and serves as the source term for SHG in the proposed Raman–OTSI cascade. For right-handed circular polarization, the nonlinear current reaches its largest amplitude under resonant, strong-magnetic-field conditions, with $|J_{NL}|$approaching unity near $r/r_0 \approx 1$and remaining large throughout the plasma channel. This enhancement originates from the resonant amplification of both the electron quiver velocity $v_1$and the ponderomotive velocity component v_2, producing a strong axial nonlinear current within the self-formed density cavity that efficiently radiates the second-harmonic mode. The resonant current profile exhibits a broad off-axis maximum determined by the Gaussian laser intensity distribution and the corresponding ponderomotive potential, followed by a gradual decay beyond the laser spot radius r_0. At lower cyclotron frequencies, the nonlinear current decreases but remains substantial, indicating that moderate magnetization still supports efficient nonlinear current generation when the laser polarization and electron gyromotion remain synchronized. In contrast, left-handed circular polarization produces much weaker currents, with $|J_{NL}| < 0.3$ across the channel and nearly flat radial profiles, particularly at larger ω_c. This behavior results from detuned cyclotron resonance, which reduces the electron velocity perturbation and weakens density modulation within the plasma channel. The polarization dependence follows the trends observed in the previous analytical results: stronger ponderomotive channel formation together with enhanced BRS and OTSI produces larger plasma-wave amplitudes and density perturbations, leading to stronger nonlinear current generation. The off-axis current maximum also indicates efficient spatial overlap with the backscattered electromagnetic field propagating inside the plasma channel.

The normalized amplitude of the second-harmonic electromagnetic field, $|E_2|/E_0$, obtained from Maxwell's equations using the analytically calculated nonlinear current density, is presented in Fig. 11. The results represent the final stage of the proposed Raman–OTSI cascade in a magnetized plasma channel. For right-handed circular polarization, the second-harmonic amplitude increases continuously with cyclotron frequency, rising from approximately 0.6 at weak magnetization to nearly unity under strong resonant conditions. This behavior reflects the sequential amplification mechanism established throughout the analytical model: cyclotron resonance strengthens the ponderomotive force, enhances BRS-driven plasma-wave excitation, promotes OTSI growth, and increases the nonlinear current responsible for second-harmonic radiation. The monotonic increase with ω_c/ω_0indicates progressively stronger coupling between the nonlinear current and the radiated electromagnetic field. At large cyclotron frequencies, second-harmonic amplitudes approaching the pump level indicate highly efficient energy

conversion following saturation of the instability cascade. In contrast, left-handed circular polarization produces substantially smaller field amplitudes that remain nearly constant over the entire magnetic-field range. The absence of cyclotron resonance suppresses plasma-channel formation, reduces BRS and OTSI growth, and limits nonlinear current generation, resulting in weak second-harmonic emission. These results demonstrate that the cyclotron frequency and laser polarization jointly determine the efficiency of SHG in magnetized plasma. Resonant conditions support strong multi-peak scattering associated with efficient harmonic generation, whereas non-resonant configurations suppress secondary emission and favor stable single-peak propagation.

The dependence of the normalized second-harmonic amplitude, $| E_2 |/E_0$, on the normalized plasma-density fluctuation, $\delta n/n_0$, is presented in Fig. 12. These results characterize the stability of nonlinear current-driven SHG in inhomogeneous plasma channels through the analytical dispersion and source equations. For all polarization and magnetization conditions, the second-harmonic amplitude decreases monotonically as the density fluctuation increases, falling from approximately unity at $\delta n/n_0 = 0$to nearly zero at $\delta n/n_0 \approx 0.4 - 0.5$. The reduction originates from the disruption of phase matching and nonlinear-current coherence, as density inhomogeneities scatter plasma waves, detune the OTSI-driven nonlinear source, and weaken coherent second-harmonic radiation. The degradation rate depends strongly on the resonance condition. For right-handed circular polarization, the second-harmonic amplitude remains comparatively robust against moderate density fluctuations. Under resonant strong-field conditions, the decay is slower because deeper plasma channels and stronger nonlinear currents maintain efficient coupling despite moderate plasma inhomogeneity. Even at $\delta n/n_0 \approx 0.2$, the resonant configuration retains $| E_2 |/E_0 > 0.6 - 0.7$, indicating that detectable SHG can persist in moderately turbulent plasmas. The weak-field right-handed case exhibits a faster decay, demonstrating the stabilizing influence of cyclotron resonance on nonlinear-current coherence. In contrast, left-handed circular polarization is highly sensitive to density fluctuations. Even for $\delta n/n_0 < 0.1$, the second-harmonic amplitude decreases rapidly, approaching zero near $\delta n/n_0 \approx 0.3$. This behavior reflects the weaker nonlinear current and shallower plasma channel produced under non-resonant conditions, making the emitted field more susceptible to scattering and phase decoherence. The nearly identical decay observed for weak and strong magnetic fields under left-handed polarization indicates that polarization mismatch dominates over magnetic-field strength in determining robustness against plasma inhomogeneity. These trends demonstrate that resonant right-handed configurations preserve efficient SHG for moderate density fluctuations, whereas non-resonant configurations require highly uniform plasmas to sustain detectable harmonic emission. These results are consistent with experimental observations showing enhanced second-harmonic electric-field amplitudes for circular polarization under cyclotron-resonant conditions [40].

The dependence of the normalized second-harmonic amplitude on the normalized wave number for different cyclotron frequencies is presented in Fig. 13. The results demonstrate that the external magnetic field governs the resonance characteristics of SHG in a magnetized plasma channel. Lorentzian-like resonance peaks shift toward larger wave numbers and broaden progressively as the cyclotron frequency increases. Under moderate and strong magnetic fields, the peak amplitude exceeds $0.9 - 1.0$, indicating highly efficient nonlinear conversion. This resonance behavior

follows from the magnetized dispersion relation, where the external magnetic field modifies the plasma susceptibility and improves phase matching between the nonlinear current source and the radiated second-harmonic field. For weak magnetic fields, the resonance remains narrow and centered near $k_2/(2k_0) \approx 1$, producing relatively small field amplitudes because cyclotron effects are weak. Increasing $\omega_c$shifts the resonance toward higher wave numbers and broadens the response, reflecting stronger ponderomotive channel formation, enhanced BRS-driven plasma-wave amplification, OTSI development, and increased nonlinear-current generation over a wider wave-number range. The strongest magnetic field produces the broadest and highest resonance peak, indicating maximum coupling efficiency between the nonlinear current and the radiated harmonic field. The systematic resonance shift demonstrates that cyclotron resonance provides an effective mechanism for tuning the emission wave number while relaxing the phase-matching condition through the modified magnetized plasma response. These results are consistent with the enhanced nonlinear-current generation and SHG efficiency obtained in the preceding analytical results, confirming that magnetization optimizes both the emission wave number and harmonic-conversion efficiency. Experimental verification of these predictions can be pursued using intense circularly polarized laser pulses interacting with underdense magnetized plasmas at multi-petawatt facilities such as ELI-NP [41, 42]. The generated second-harmonic radiation can be measured using backscattered and EUV spectrometers together with Thomson-scattering diagnostics, as demonstrated in recent experiments on stimulated Raman rescattering, harmonic generation in magnetized plasmas, and Raman-assisted SHG.

The saturation amplitude of the second-harmonic electromagnetic mode as a function of the normalized cyclotron frequency is presented in Fig. 14. The results represent the steady-state response established after nonlinear saturation of the BRS–OTSI cascade, where particle trapping and pump depletion limit further instability growth. The saturation behavior agrees with the kinetic features observed in the EPOCH PIC simulations and exhibits a pronounced dependence on laser polarization and magnetic-field strength. For right-handed circular polarization, the saturation amplitude displays a distinct maximum exceeding 0.9–1.0 at intermediate cyclotron frequencies. The weak-field case reaches the highest peak near unity before gradually decreasing, whereas stronger magnetic fields maintain saturation levels of approximately 0.8–0.9 over a broader frequency range. This behavior indicates that intermediate magnetization provides efficient plasma-channel formation and nonlinear-current generation while avoiding excessive suppression of longitudinal plasma-wave growth. In contrast, left-handed circular polarization produces lower and broader saturation profiles, with the maximum shifted toward higher cyclotron frequencies. The absence of cyclotron resonance weakens the BRS–OTSI cascade, resulting in smaller nonlinear currents and earlier saturation. At large cyclotron frequencies, the saturation amplitude decreases for both polarizations because strong magnetization suppresses longitudinal plasma-wave excitation, reducing OTSI growth and the associated nonlinear current. These results demonstrate that the steady-state SHG efficiency is governed by the combined effects of laser polarization and magnetic-field strength, with resonant intermediate magnetization providing the highest saturation amplitude.

IV. Conclusions

The present work provides a theoretical and numerical investigation of the nonlinear mechanisms responsible for multi-peak BRS in magnetized plasma channels driven by intense circularly polarized laser pulses. The analytical fluid model demonstrates that the secondary spectral peak originates from a well-defined nonlinear cascade in which ponderomotive channel formation and resonant electron quiver motion first amplify plasma waves through BRS. The amplified Langmuir wave subsequently drives OTSI, generating density perturbations and nonlinear axial currents that radiate the second-harmonic electromagnetic mode. The efficiency of this cascade is governed by laser polarization handedness and cyclotron resonance. Right-handed circular polarization, co-rotating with the electron gyromotion, enhances the ponderomotive force, plasma-channel formation, instability growth, nonlinear current generation, and SHG, whereas left-handed polarization suppresses these processes because of detuned cyclotron resonance.

Macroscopic COMSOL simulations are consistent with the analytical model, reproducing the dependence of plasma-channel evolution and instability development on laser wavelength, pulse duration, plasma density, and magnetic-field strength. The analytical results further show that resonant configurations maintain efficient SHG under moderate plasma-density fluctuations and provide magnetic-field-controlled tuning of the emitted harmonic spectrum. Fully kinetic PIC simulations performed with the EPOCH code provide a complementary description of the same physical process by resolving electron phase-space dynamics beyond the fluid approximation. The simulations capture particle trapping, velocity-space bunching, and phase-space vortex formation associated with OTSI, supporting the proposed BRS–OTSI cascade. The agreement between the analytical predictions, COMSOL simulations, and PIC results indicates that the observed multi-peak Raman structure is a robust consequence of nonlinear laser-plasma interaction rather than a numerical artifact. The results identify cyclotron resonance and laser polarization as experimentally accessible parameters for controlling nonlinear Raman scattering and SHG in magnetized plasmas. This mechanism provides a framework for designing tunable harmonic radiation sources and investigating nonlinear energy-transfer processes in high-intensity laser-plasma interactions.

Acknowledgment & Funding

This work did not receive any specific grant from funding agencies in the public, commercial, or not-for-profit sectors.

Author Contributions

A. A. Molavi Choobini was responsible for conceptualization, data curation, Software, formal analysis, investigation, methodology, writing the original draft, review and editing.

S. S. Ghaffari-Oskooei contributed equally to investigation, project administration, validation, and review and editing of the manuscript

Declaration of competing interest

The authors declare that they have no known competing financial interests or personal relationships that could have appeared to influence the work reported in this paper.

Data availability

The data and computational codes supporting the findings of this study are available from the corresponding author upon reasonable request.

References

[1] D. E. Rivas, A. Borot, D. E. Cardenas, G. Marcus, X. Gu, D. Herrmann, J. Xu, J. Tan, D. Kormin, G. Ma and W. Dallari, "Next Generation Driver for Attosecond and Laser-plasma Physics." Sci Rep., 7(1), 5224, (2017).

[2] P. Lassonde, H. Ibrahim, A. Leblanc, J. Azaña, B. E. Schmidt and F. Légaré, "Information transfer via temporal convolution in nonlinear optics." Sci Rep., 10(1), 14969, (2020).

[3] M. Garg, A. Martin-Jimenez, Y. Luo, and K. Kern, "Ultrafast Photon-Induced Tunneling Microscopy." ACS Nano., 15(11), 18071-18084, (2021).

[4] A. A. Molavi Choobini and S. S. Ghaffar-Oskooei "Two-plasmon decay instability and 3/2 harmonic generation in inhomogeneous magnetized plasma." Journal of the Optical Society of America B, 42(7), (2025).

[5] F. Ding, Y. Yi, P. Zhu, X. Zhang, D. Zhang, X. Ouyang, X. Xie and J. Zhu, "Single-shot complete characterization of synthesized laser pulses and the nonlinear frequency-conversion process." Opt Express., 32(14), 24262-24274, (2024).

[6] Y. Zhao, Z. Chen, C. Wang, Y. Yang and H. B. Sun, "Efficient second- and higher-order harmonic generation from $LiNbO_3$ metasurfaces." Nanoscale., 15(31), 12926-12932, (2023).

[7] D. Jang and K. Y. Kim, "Multicycle terahertz pulse generation by optical rectification in $LiNbO_3$, $LiTaO_3$, and BBO crystals." Opt Express., 28(14), 21220-21235, (2020).

[8] W. Geng, Y. Fang, Y. Wang, C. Bao, W. Liu, Z. Pan and Y. Yue, "Nonlinear photonics on integrated platforms." Nanophotonics., 13(18), 3253-3278, (2024).

[9] M. A. Adeshina and H. Kim "Exploring the frontier: nonlinear optics in low dimensional materials." Nanophotonics., 14(10), 1451-1473, (2025).

[10] Y. Zhao, S. Weng, Z. Sheng, N. Kang, H. Liu, J. Zhu and J. Zhang, "Plasma modulator for high-power intense lasers." Opt Express., 28(11), 15794-15804, (2020).

[11] M. R. Edwards and J. M Mikhailova, " The X-Ray Emission Effectiveness of Plasma Mirrors: Reexamining Power-Law Scaling for Relativistic High-Order Harmonic Generation." Sci Rep., 10(1), 5154, (2020).

[12] L. Chopineau, A. Denoeud, A. Leblanc, E. Porat, P. Martin, H. Vincenti and F. Quéré, "Spatio-temporal characterization of attosecond pulses from plasma mirrors." Nature Physics., 17(8), 968-973, (2021).

[13] E. Oks, E. Dalimier, A. Faenov, T. Pikuz, Y. Fukuda, A. Andreev, J. Koga, H. Sakaki, H. Kotaki, A. Pirozhkov and Y. Hayashi, " Revealing the second harmonic generation in a femtosecond laser-driven cluster-based plasma by analyzing shapes of Ar XVII spectral lines." Optics Express, 23, 25, (2015).

[14] A. S. Ahmed, H. A. Salih and K. I. Hassoon, "q-Gaussian laser beam for second-harmonic generation from unmagnetized plasma." J Opt, 53(2), 1328–1335, (2024).

[15] N. Gupta, S. B. Bhardwaj, S. Kumar, S. Choudhry, R. Khatri, S. Shishodia and R. Johari, "Second-harmonic generation of two cross-focused q-Gaussian laser beams by nonlinear frequency mixing in plasmas." J Opt, 53(1), 18–29, (2024).

[16] K. Walia, "Nonlinear Dynamics of Intense Laser Beam in Unmagnetized Plasma and its Influence on Second Harmonic Generation." Journal of Fusion Energy, 41:21, (2022).

[17] V. Sharma, V. Thakur, S. Srivastava and N. Kant, "Resonant second-harmonic generation of self-focused oblique incident laser beam in plasma." Laser Phys. 34, 035401 (7pp), (2024).

[18] R. A. Ganeev, "High-order harmonics enhancement in laser-induced plasma." Scientific Reports, 13, 13951, (2023).

[19] N. F. Beierand F. Dollar, "Two-color high-harmonic generation from relativistic plasma mirrors." Physical Review E, 108, 015201 (2023).

[20] J. Mathijssen, E. J. Salumbides, K. S. Eikema and S. Witte, "Sub-cycle dynamics in two-color high-harmonic generation from laser-produced plasmas." Optics Express, 32, 17, 30824, (2024).

[21] K. J. Garriga Francis, M. L. Pac Chong, E. Yiwen and X. C. Zhang, "Observation of strong terahertz field-induced second harmonic generation in plasma filaments." Optics Letters, 47, 23, 6297, (2022).

[22] K. J. G. Francis and X. Ch. Zhang, "Local measurement of terahertz field-induced second harmonic generation in plasma filaments." Frontiers of Optoelectronics,16, 44, (2023).

[23] M. L. Pac Chong, K. J. Garriga Francis, E. Yiwen and X. C. Zhang, "Single-shot local measurement of terahertz correlated second harmonic generation in laser air plasma filaments." Optics Letters, 49, 2, (2024).

[24] C. K. Huang, C. Zhang, Z. Nie, K. A. Marsh, C. E. Clayton and C. Joshi, "Conservation of angular momentum in second harmonic generation from under-dense plasmas." Communication Physics, 3, 213, (2020).

[25] S. Y. Fu, K. J. Garriga Francis, M. L. Pac Chong, E. Yiwen and X. C. Zhang, "Enhanced second harmonic generation in laser-induced air plasma." Optics Letters, 48, 12, 3199, (2024).

[26] Y. H. Kim, H. Kim, S. C. Park, Y. Kwon, K. Yeom, W. Cho, T. Kwon, H. Yun, J. H. Sung, S. K. Lee and T. T. Luu, "High-harmonic generation from a flat liquid-sheet plasma mirror." Nature Communications, 14, 2328, (2023).

[27] Sh. Takeyama, E. Kojima, "A copper-lined magnet coil with maximum field of 700 T for electromagnetic flux compression." J. Phys. D: Appl. Phys. 44 425003, (2011).

[28] A. S. Prasad, R. Ravishankar, B. Büchner, V. Neu, Th. Mühl, " Micron sized coils for the generation of high magnetic fields and field gradients." Nature, Commun Mater 6, 164, (2025).

[29] S. S. Ghaffari-Oskooei, A. A. Molavi Choobini, "Forward Raman scattering and self-modulation instabilities of lasers in magnetized tapered plasma channels." Physics Letters A, 559, 130942, (2025).

[30] M. Luo, S. Hüller, M. Chen, Zh. Sheng, "On the role of bandwidth in pump and seed light waves for stimulated Raman scattering in inhomogeneous plasmas." Phys. Plasmas 29, 032102 (2022).

[31] C. S. Liu and V. K. Tripathi, " Second-harmonic generation of Raman scattered light in a plasma channel." PHYSICAL REVIEW E, 54, 4, (1996).

[32] D. N. Gupta, K. Singh, A. Sharma, N. K. Jaiman, " Nonlinear saturation of laser driven plasma beat wave by oscillating two-stream instability." Physics of Plasma, 11(11):5250-5255, (2004).

[33] N. Ahmad, V. Tripathi, M. Ahmad, M. Rafat, " Oscillating two-stream instability of laser wakefield-driven plasma wave." Pramana 86(1):157-167, (2015).

[34] W. Yao, A. Higginson, J. R. Marquès, P. Antici, J. Béard, K. Burdonov, M. Borghesi, A. Castan, A. Ciardi, B. Coleman and Chen, S.N "Dynamics of nanosecond laser pulse propagation and of associated instabilities in a magnetized underdense plasma." arXiv, (2022).

[35] M. Bailly-Grandvaux, B. J. Winjum, M. E. Manuel, S. Bolaños, C. A. Walsh, J. Saret, A. Bogale, J. Strehlow, R. Lee, F. Tsung and W. Mori "Validation of magnetized gas-jet experiments to investigate the effects of an external magnetic field on laser-plasma instabilities." J. Plasma Phys., vol. 89, 175890201, (2023).

[36] I. Tazes, S. Passalidis, E. Kaselouris, D. Mancelli, C. Karvounis, A. Skoulakis, I. Fitilis, M. Bakarezos, N. A. Papadogiannis, V. Dimitriou and M. Tatarakis, "Efficient Magnetic Vortex Acceleration by femtosecond laser interaction with long living optically shaped gas targets in the near critical density plasma regime." Scientific Reports, 14:4945, (2024).

[37] S. Bolaños, M. Bailly-Grandvaux, B. J. Winjum, M. E. Manuel, A. Bogale, T. Filkins, D. H. Froula, R. Lee, W. Mori, F. Tsung and C. A. Walsh "Direct evidence of the effect of a moderate external magnetic field on stimulated Raman scattering in the kinetic regime." Phys. Plasmas 32, 092102 (2025).

[38] T. D. Arber, K. Bennett, C. S. Brady, A. Lawrence-Douglas, M. G. Ramsay, N. J. Sircombe, P. Gillies, R. G. Evans, H. Schmitz, A. R. Bell and C. P. Ridgers, "Contemporary particle-in-cell approach to laser-plasma modelling," Plasma Phys. Control. Fusion 57 113001, (2015).

[39] J. R. Marquès, F. Pérez, P. Loiseau, L. Lancia, C. Briand, S. Depierreux, M. Grech and C. Riconda, "Experimental evidence of stimulated Raman re-scattering in laser-plasma interaction." arXiv, (2025).

[40] G. Cristoforetti, S. Hüller, P. Koester, L. Antonelli, S. Atzeni, F. Baffigi, D. Batani, C. Baird, N. Booth, M. Galimberti and K. Glize, "Observation and modelling of stimulated Raman scattering driven by an optically smoothed laser beam in experimental conditions relevant for shock ignition." High Power Laser Science and Engineering, 9, e60, (2021).

[41] K. Krushelnick, A. Ting, H. R. Burris, A. Fisher, C. Manka, and E. Esarey, "Second harmonic generation of stimulated Raman scattered light in underdense plasmas," Phys. Rev. Lett. 75, 3681 (1995).

[42] J.-R. Marquès, F. Pérez, P. Loiseau, L. Lancia, C. Briand, S. Depierreux, M. Grech, and C. Riconda, "Experimental evidence of stimulated Raman re-scattering in laser-plasma interaction," Phys. Rev. Lett. 135, 105101, (2025).

List of Figures & Captions

Fig. 1. Schematic illustration of the interaction of a circularly polarized laser pulse with a magnetized plasma channel, leading to axial current modulation and efficient second-harmonic generation.

Fig. 2. Normalized electric field amplitude ($|E_z|/E_0$) of a circularly polarized Gaussian laser pulse as a function of normalized radial distance r/r_0 in a magnetized plasma channel for various laser wavelengths.

Fig. 3. Impact of pulse duration of laser pulse on normalized electric field amplitude ($|E_z|/E_0$) of a circularly polarized Gaussian laser pulse as a function of normalized radial distance r/r_0 in a magnetized plasma channel.

Fig. 4. Effect of plasma densities on normalized electric field amplitude ($|E_z|/E_0$) of a circularly polarized Gaussian laser pulse as a function of normalized radial distance r/r_0 in a magnetized plasma channel.

Fig. 5. Variations of radial profile of the ponderomotive force, F_{pond} (shown in arbitrary units), as a function of normalized radial distance r/r_0 in a magnetized plasma for different polarizations at weak ($\omega_c = 0.1\omega_0$) and strong ($\omega_c = 0.9\omega_0$) electron cyclotron frequencies.

Fig. 6. Analytical profiles of plasma channelling condition (top) and corresponding radial plasma density perturbation n_s/n_0 (bottom) for laser pulse in a magnetized plasma for right-handed and left-handed polarizations at weak and strong cyclotron frequencies.

Fig. 7. Three-dimensional map of the growth rate Γ_{BRS} as a function of normalized plasma frequency ω_{pe}/ω_0 and normalized electron cyclotron frequency ω_{pe}/ω_0.

Fig. 8. Temporal evolution of the growth rate Γ_{OSTI} as a function of wave number $k(\sim 0.01 - 3 \times 10^6 m^{-1})$ and external magnetic field B_0 for four snapshots.

Fig. 9. Analytical growth rate Γ_{BRS} as a function of normalized plasma frequency ω_{pe}/ω_0 for right-handed and left-handed circular polarizations at weak and strong cyclotron frequencies.

Fig. 10. Radial profile of the normalized nonlinear current density $|J_{NL}|$ generated as a function of normalized radial distance r/r_0 in the plasma channel by a circularly polarized laser pulse.

Fig. 11. Normalized amplitude of the second-harmonic (second red-shifted) electric field $|E_2|/E_0$ generated via nonlinear current drive in the plasma channel as a function of normalized cyclotron frequency ω_c/ω_0.

Fig. 12. Normalized second-harmonic electric field amplitude $|E_2|/E_0$ versus plasma density fluctuations $\delta n/n_0$ in the magnetized channel for various circular polarizations at weak and strong cyclotron frequencies.

Fig. 13. Normalized second-harmonic electric field amplitude $|E_2|/E_0$ as a function of normalized wave number $k_2/2k_0$ of the secondary mode for various cyclotron frequencies.

Fig. 14. Saturation level of the normalized second-harmonic electric field amplitude $||E_{2,Sat}|/E_0$ as a function of normalized cyclotron frequency ω_c/ω_0 for various circular polarizations at weak and strong cyclotron frequencies.

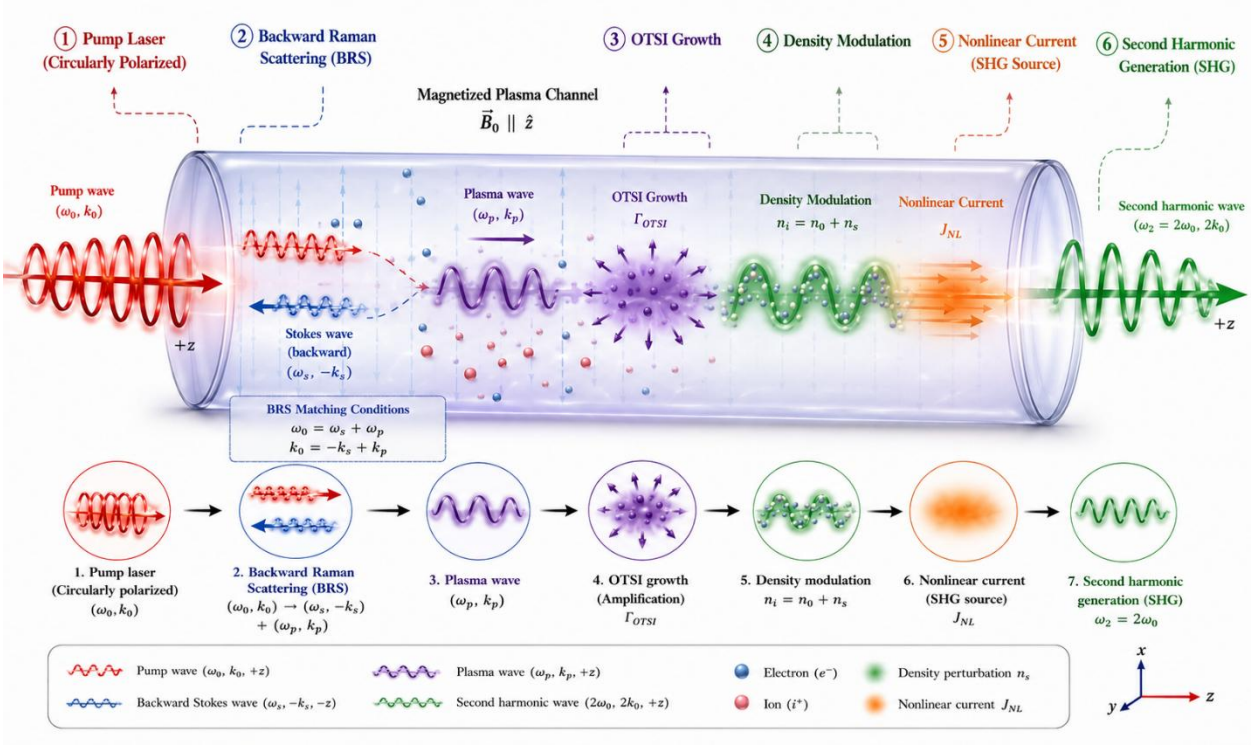


Fig. 1.

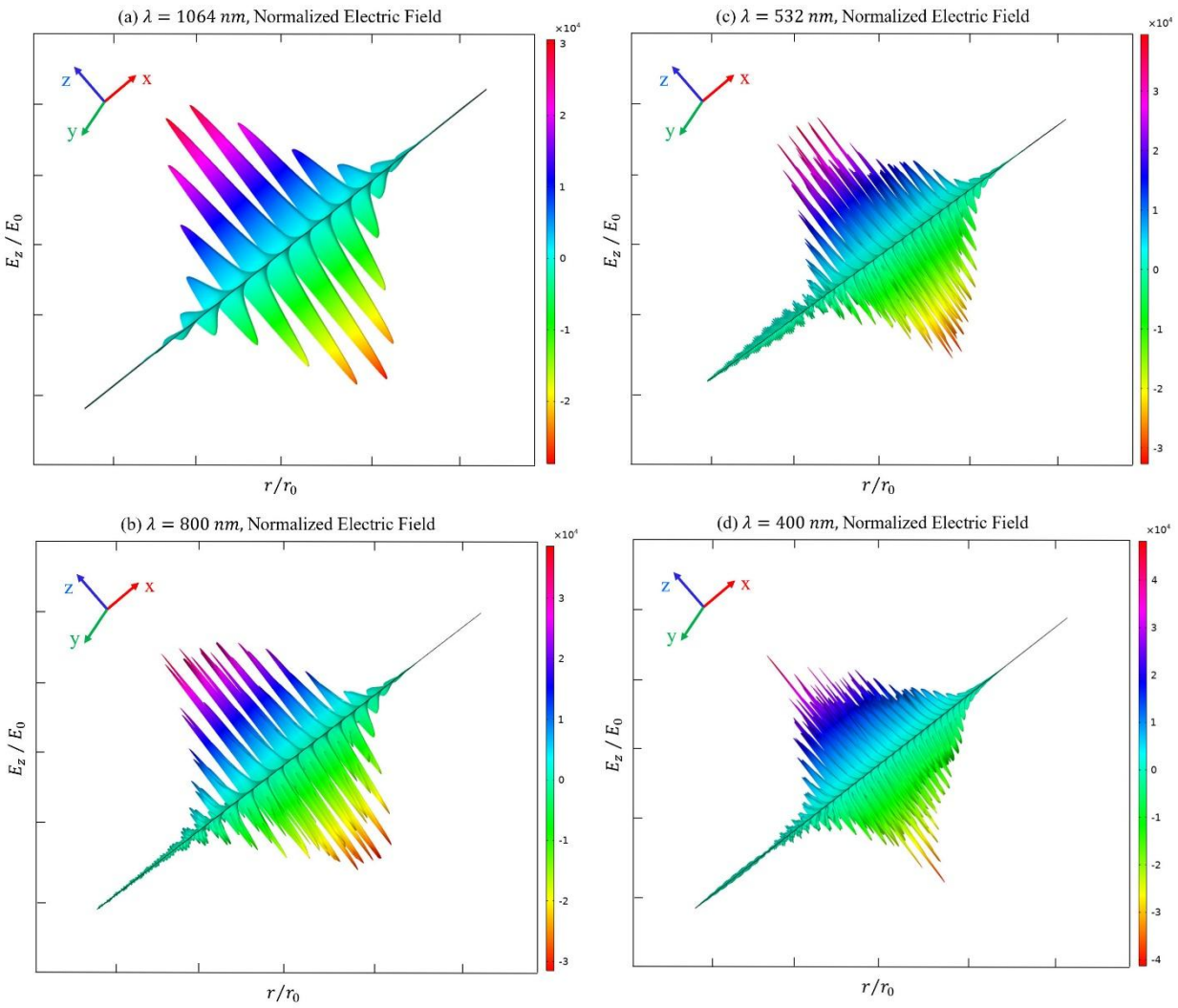

(a) $\lambda = 1064\ nm$, Normalized Electric Field
(c) $\lambda = 532\ nm$, Normalized Electric Field
(b) $\lambda = 800\ nm$, Normalized Electric Field
(d) $\lambda = 400\ nm$, Normalized Electric Field
E_z / E_0
r/r_0
x
y
z
$\times 10^4$

Fig. 2.

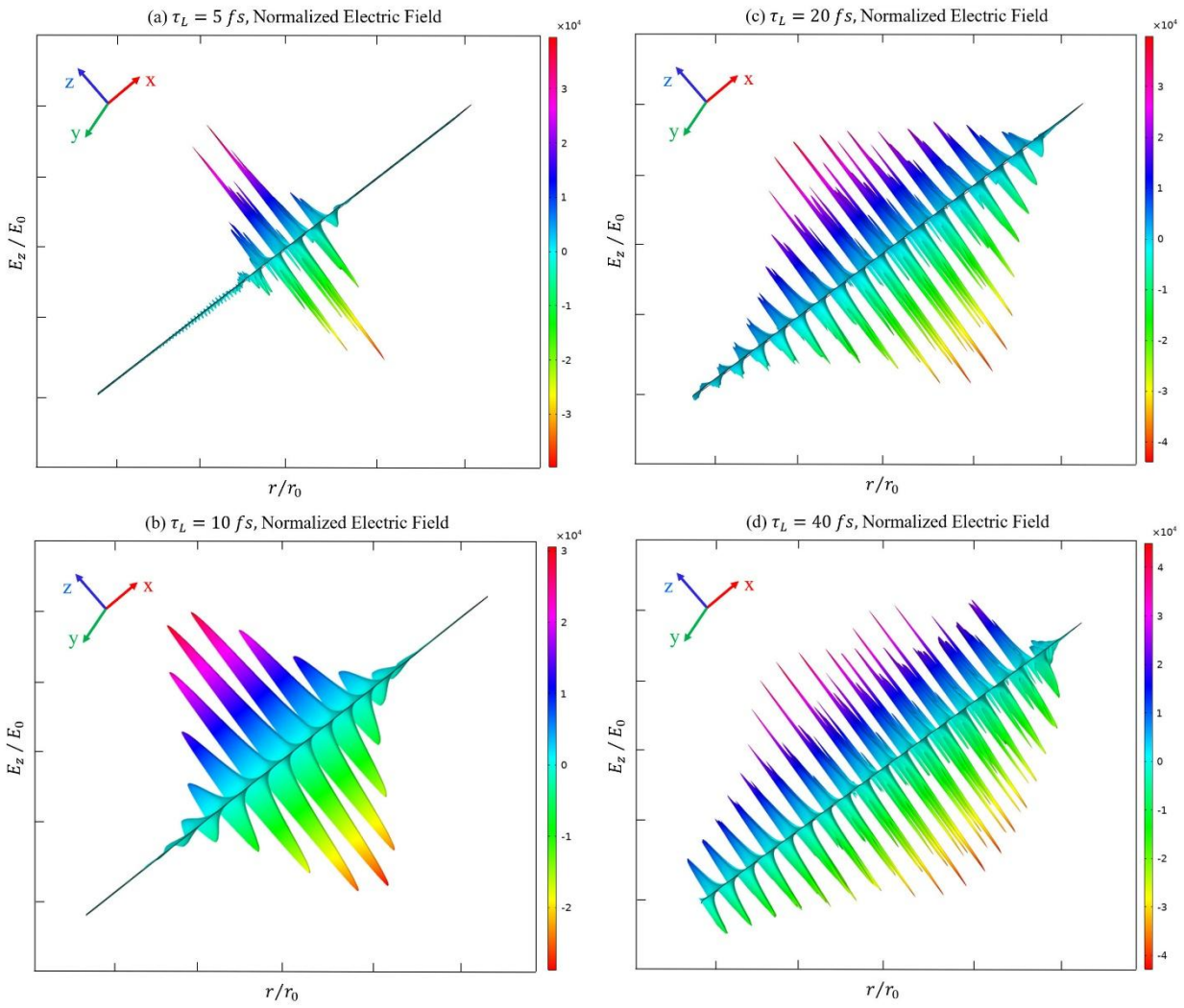

(a) $\tau_L = 5\ fs$, Normalized Electric Field
(c) $\tau_L = 20\ fs$, Normalized Electric Field
(b) $\tau_L = 10\ fs$, Normalized Electric Field
(d) $\tau_L = 40\ fs$, Normalized Electric Field
E_z / E_0
r/r_0
z
x
y
$\times 10^4$

Fig. 3.

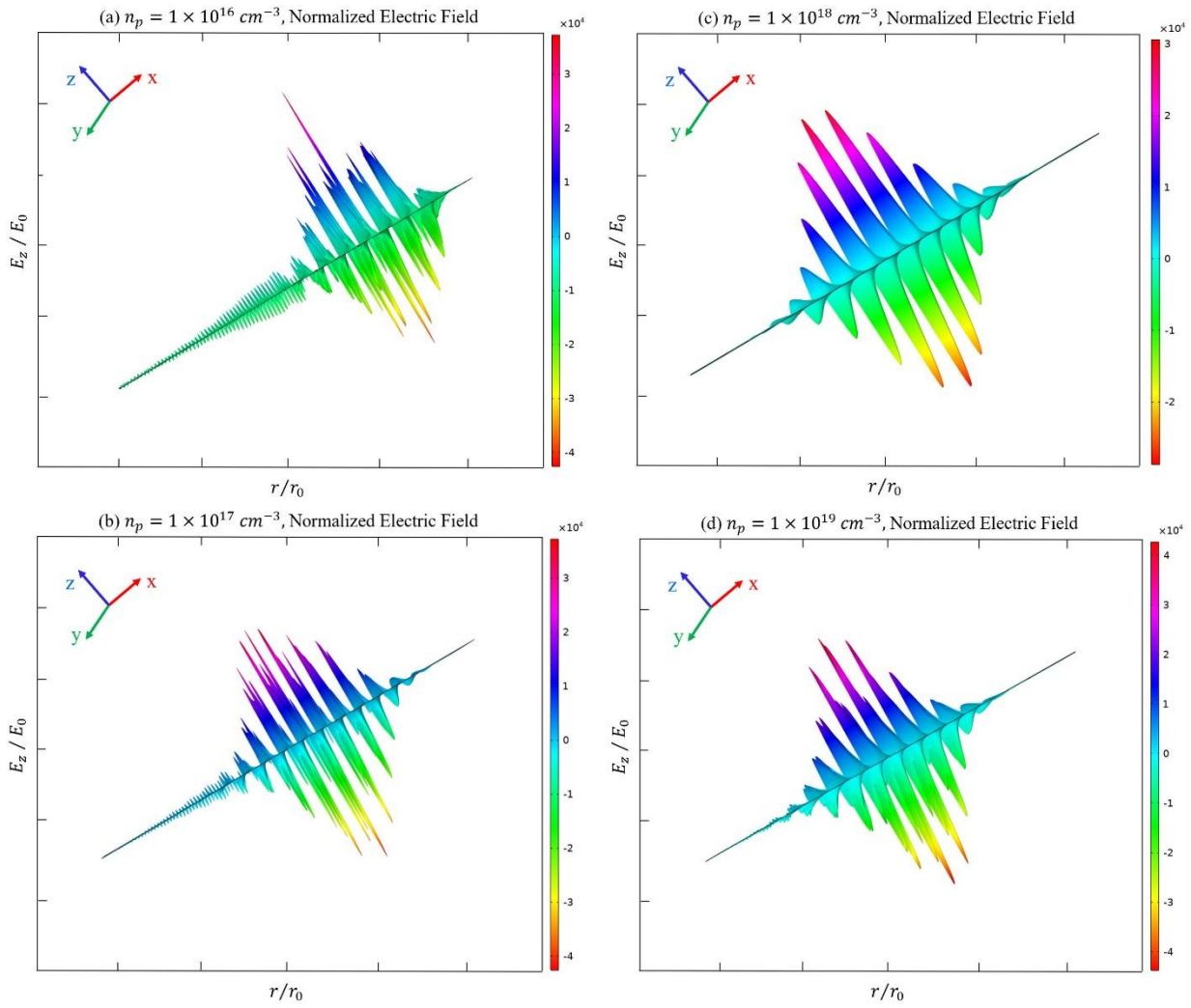

(a) $n_p = 1 \times 10^{16}\ cm^{-3}$, Normalized Electric Field
(c) $n_p = 1 \times 10^{18}\ cm^{-3}$, Normalized Electric Field
(b) $n_p = 1 \times 10^{17}\ cm^{-3}$, Normalized Electric Field
(d) $n_p = 1 \times 10^{19}\ cm^{-3}$, Normalized Electric Field
E_z / E_0
r/r_0
z
x
y
×10⁴

Fig. 4.

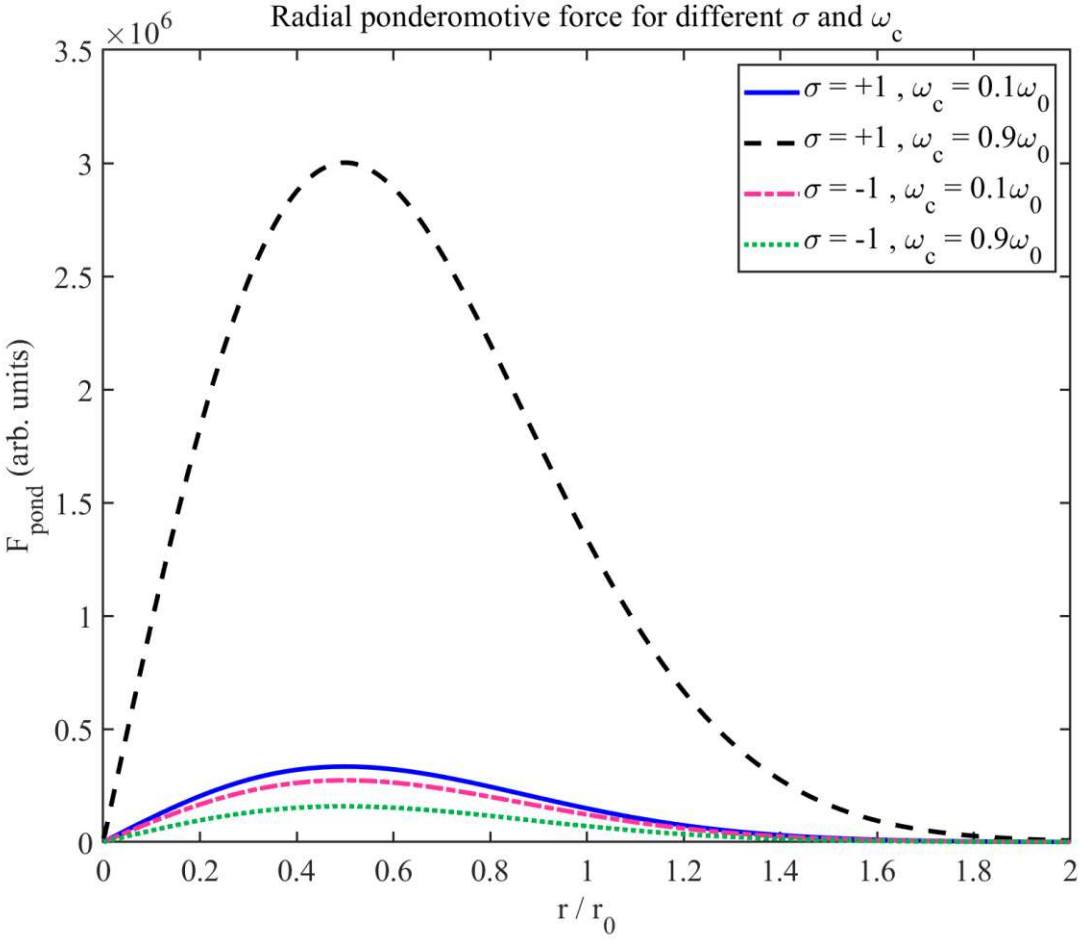
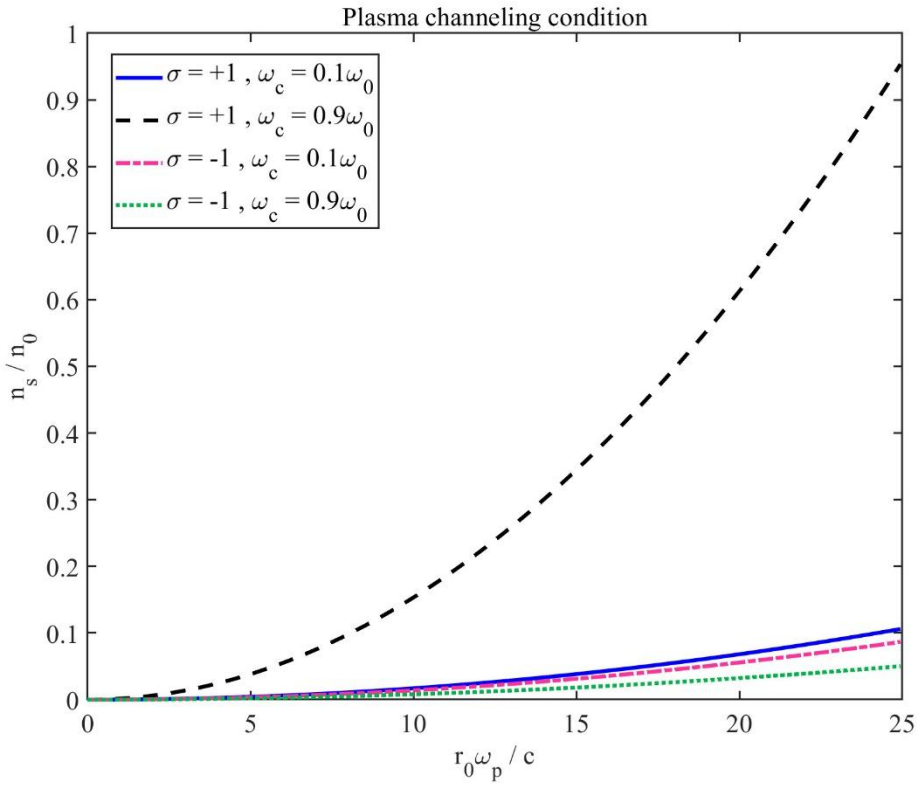

Radial ponderomotive force for different σ and ω_c
$\times 10^6$
3.5
3
2.5
2
1.5
1
0.5
0
F_{pond} (arb. units)
0
0.2
0.4
0.6
0.8
1
1.2
1.4
1.6
1.8
2
r / r_0
$\sigma = +1$, $\omega_c = 0.1\omega_0$
$\sigma = +1$, $\omega_c = 0.9\omega_0$
$\sigma = -1$, $\omega_c = 0.1\omega_0$
$\sigma = -1$, $\omega_c = 0.9\omega_0$

Fig. 5.


Plasma channeling condition
σ = +1 , ω_c = 0.1ω_0
σ = +1 , ω_c = 0.9ω_0
σ = -1 , ω_c = 0.1ω_0
σ = -1 , ω_c = 0.9ω_0
n_s / n_0
r_0ω_p / c
0
0.1
0.2
0.3
0.4
0.5
0.6
0.7
0.8
0.9
1
0
5
10
15
20
25

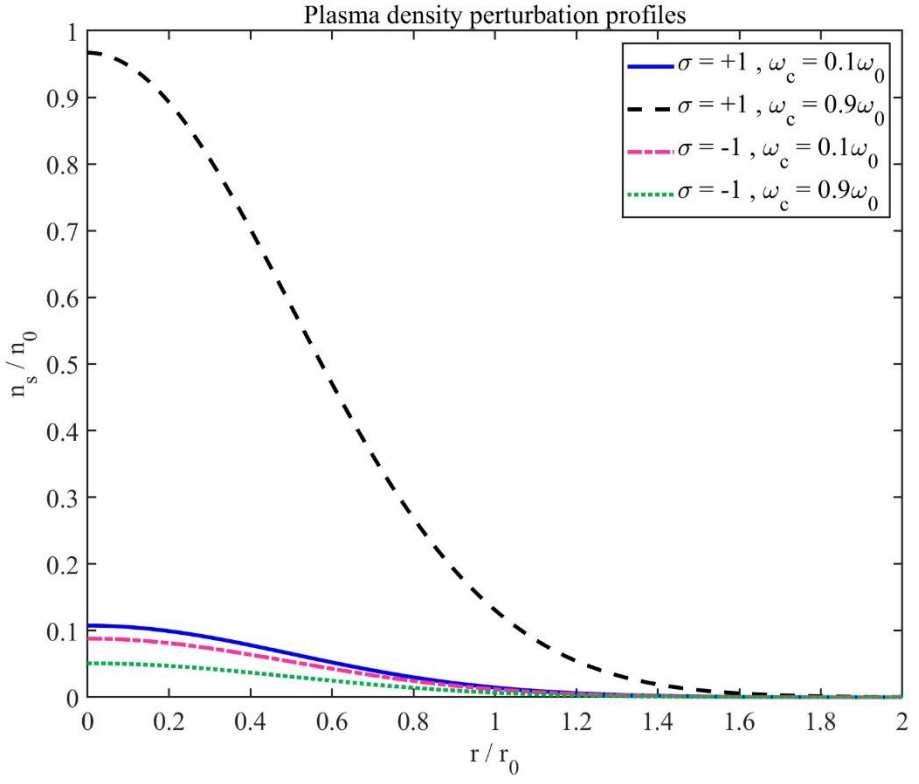

Plasma density perturbation profiles
σ = +1 , ω_c = 0.1ω_0
σ = +1 , ω_c = 0.9ω_0
σ = -1 , ω_c = 0.1ω_0
σ = -1 , ω_c = 0.9ω_0
n_s / n_0
r / r_0
0
0.1
0.2
0.3
0.4
0.5
0.6
0.7
0.8
0.9
1
0
0.2
0.4
0.6
0.8
1
1.2
1.4
1.6
1.8
2

Fig. 6.

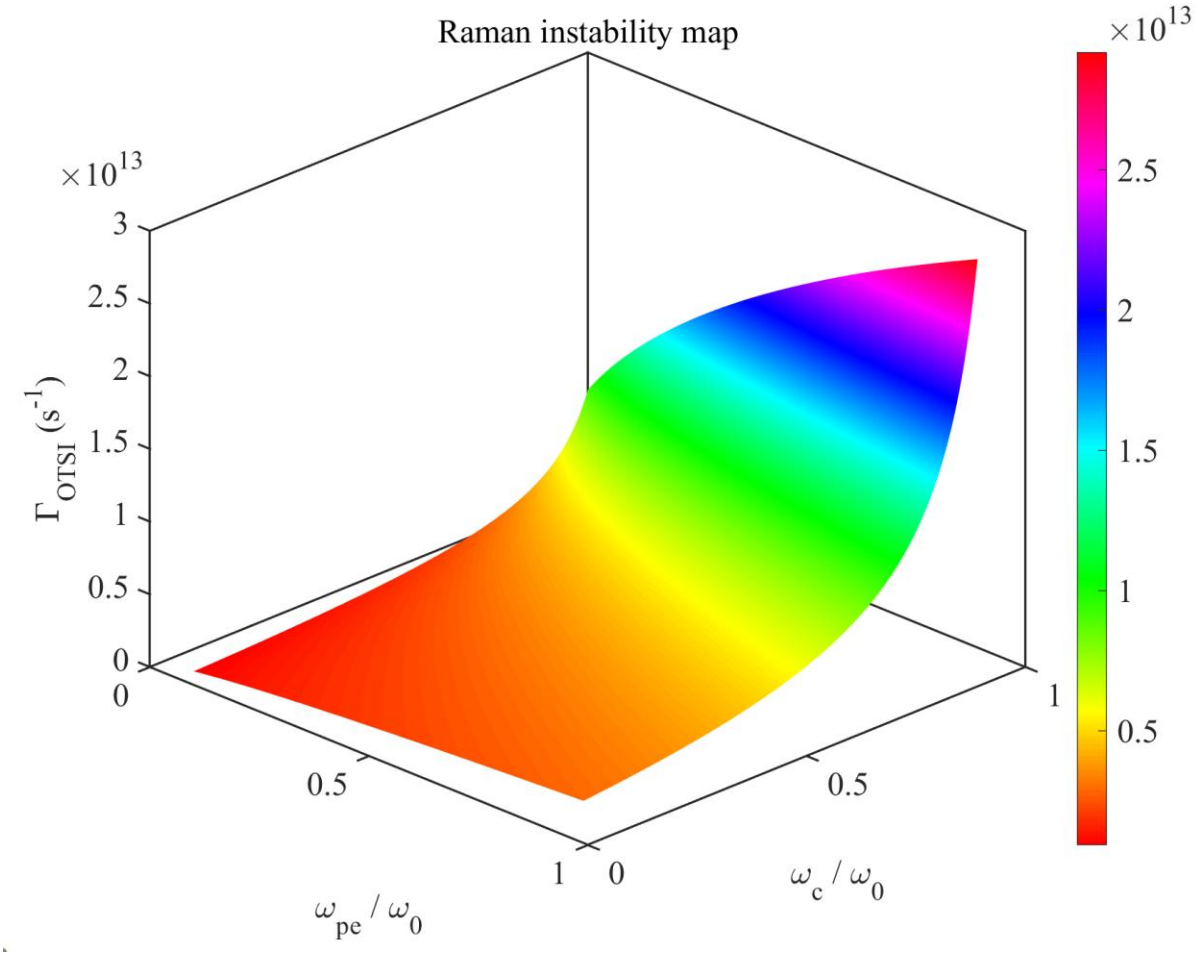

Raman instability map
×10^13
3
2.5
2
1.5
1
0.5
0
Γ_OTSI (s^-1)
0
0.5
1
ω_pe / ω_0
0
0.5
1
ω_c / ω_0
×10^13
2.5
2
1.5
1
0.5

Fig. 7.

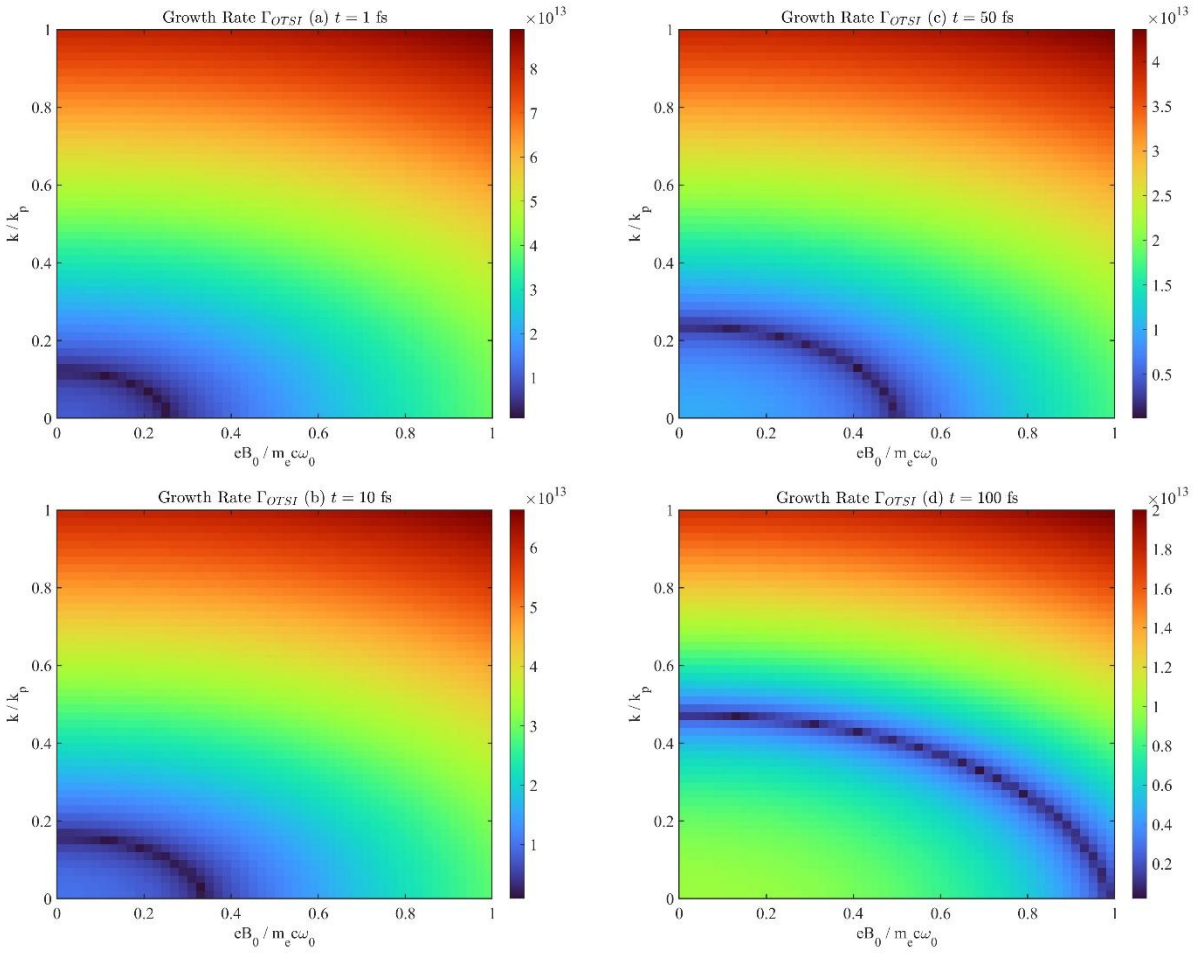

Growth Rate Γ_{OTSI} (a) $t = 1$ fs
Growth Rate Γ_{OTSI} (b) $t = 10$ fs
Growth Rate Γ_{OTSI} (c) $t = 50$ fs
Growth Rate Γ_{OTSI} (d) $t = 100$ fs
$\times 10^{13}$
k / k$_p$
eB$_0$ / m$_e$cω$_0$

Fig. 8.

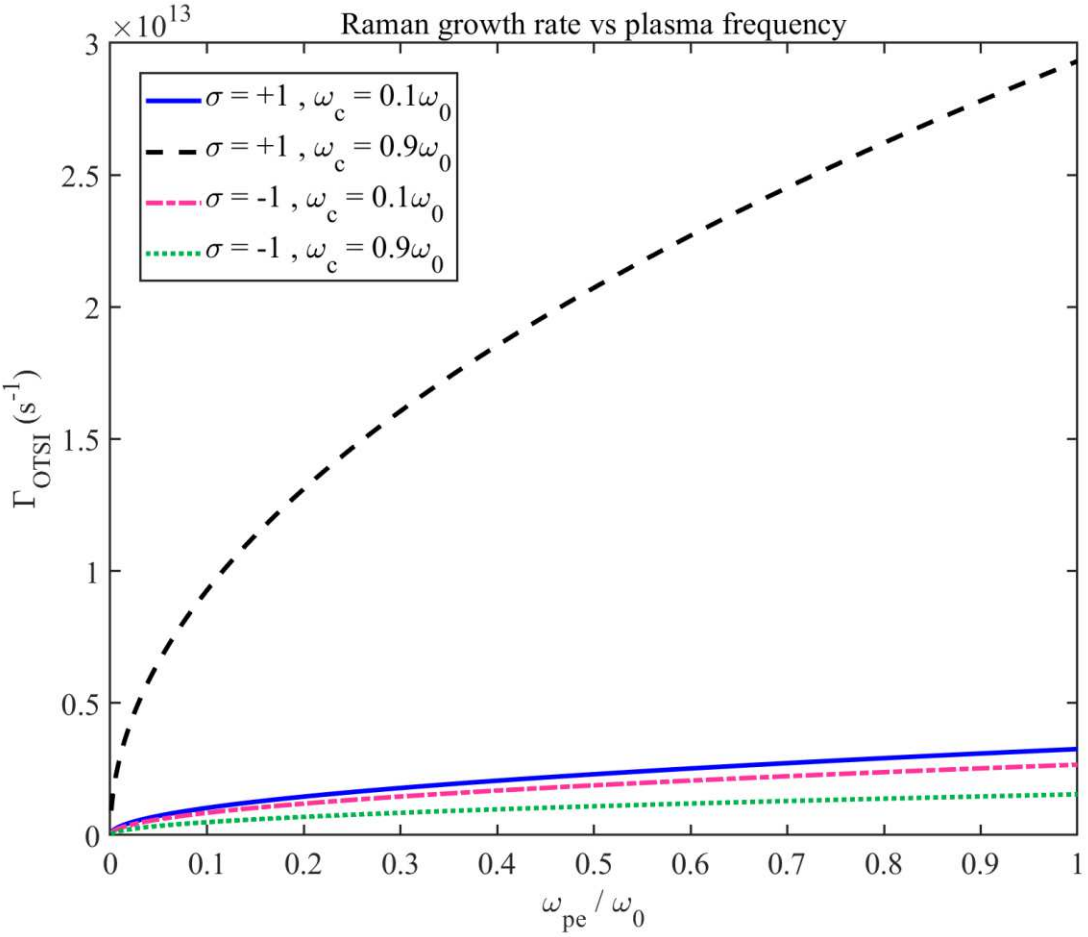

Raman growth rate vs plasma frequency
×10^13
3
2.5
2
1.5
1
0.5
0
Γ_OTSI (s^-1)
σ = +1 , ω_c = 0.1ω_0
σ = +1 , ω_c = 0.9ω_0
σ = -1 , ω_c = 0.1ω_0
σ = -1 , ω_c = 0.9ω_0
0
0.1
0.2
0.3
0.4
0.5
0.6
0.7
0.8
0.9
1
ω_pe / ω_0

Fig. 9.

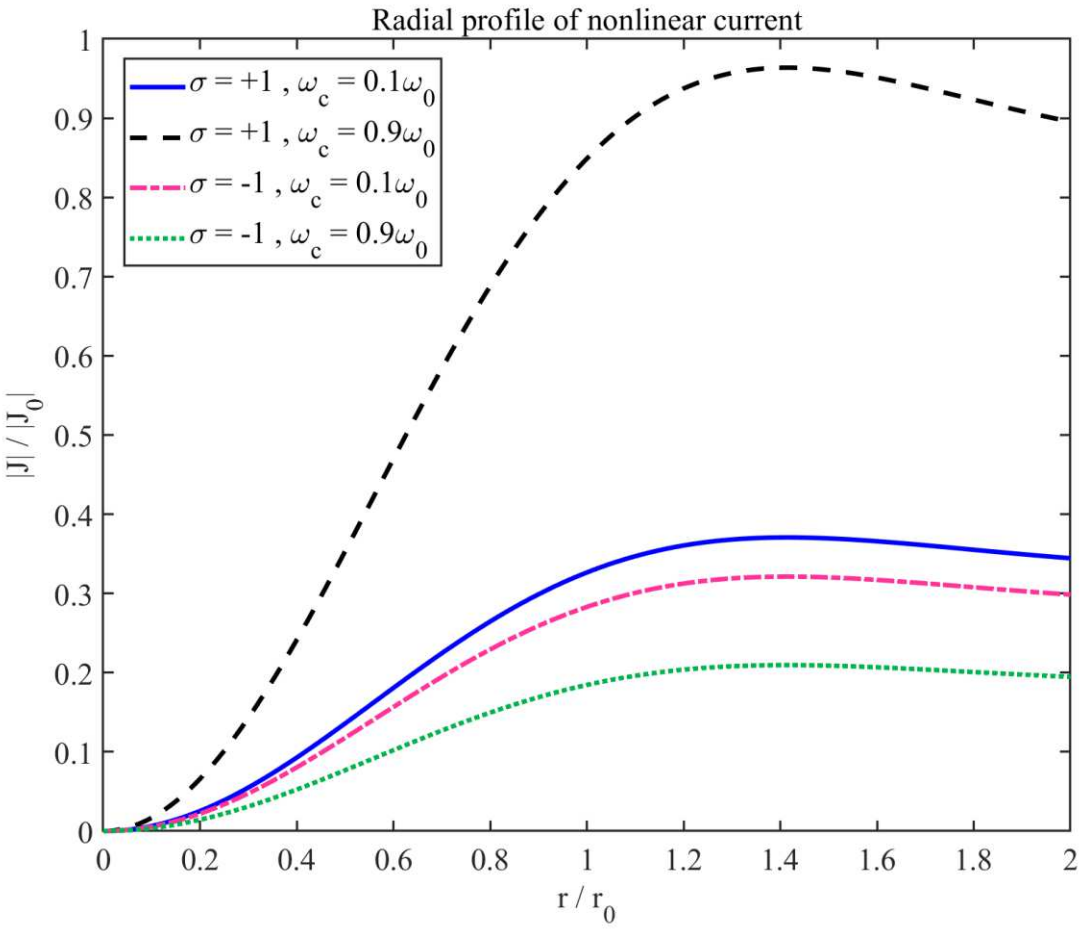

Radial profile of nonlinear current
σ = +1 , ω_c = 0.1ω_0
σ = +1 , ω_c = 0.9ω_0
σ = -1 , ω_c = 0.1ω_0
σ = -1 , ω_c = 0.9ω_0
|J| / |J_0|
r / r_0
0
0.1
0.2
0.3
0.4
0.5
0.6
0.7
0.8
0.9
1
0.2
0.4
0.6
0.8
1.2
1.4
1.6
1.8
2

Fig. 10.

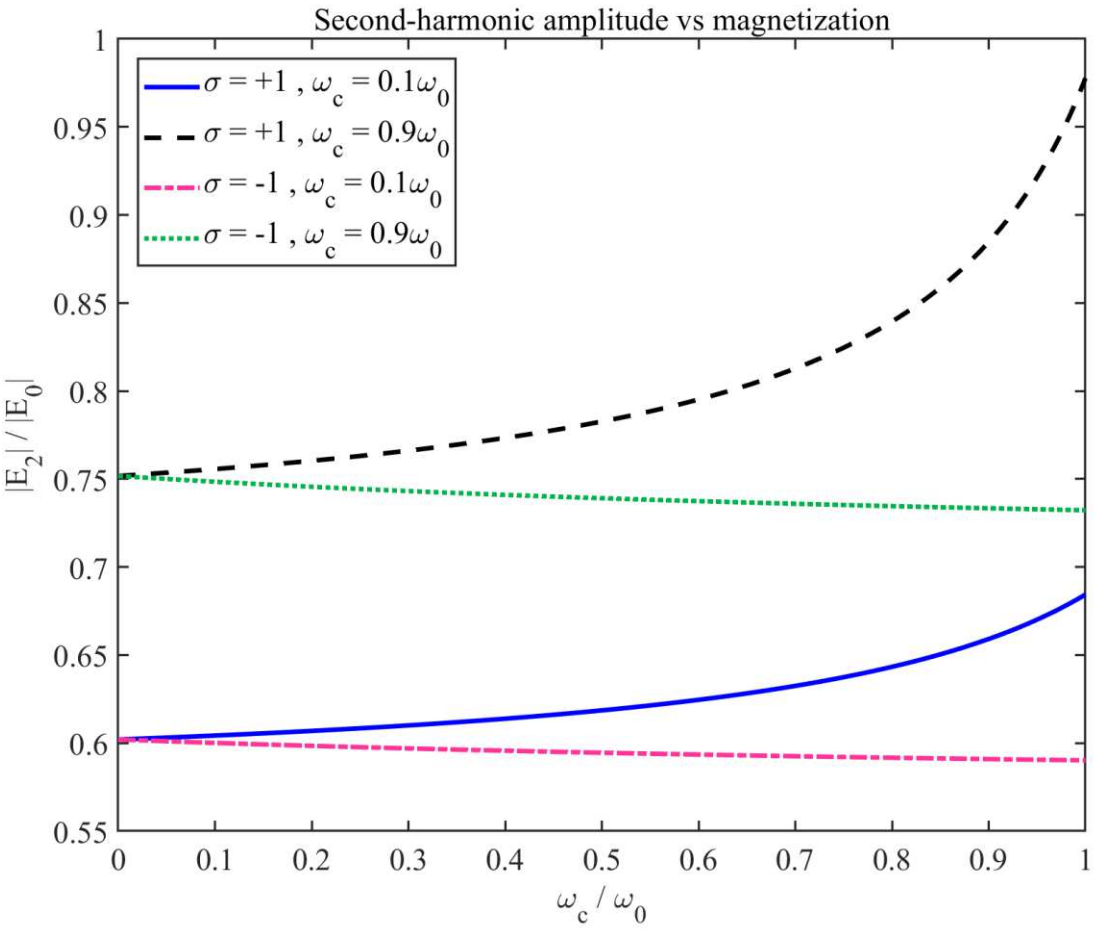

Second-harmonic amplitude vs magnetization
σ = +1 , ω_c = 0.1ω_0
σ = +1 , ω_c = 0.9ω_0
σ = -1 , ω_c = 0.1ω_0
σ = -1 , ω_c = 0.9ω_0
|E_2| / |E_0|
ω_c / ω_0
1
0.95
0.9
0.85
0.8
0.75
0.7
0.65
0.6
0.55
0
0.1
0.2
0.3
0.4
0.5
0.6
0.7
0.8
0.9
1

Fig. 11.

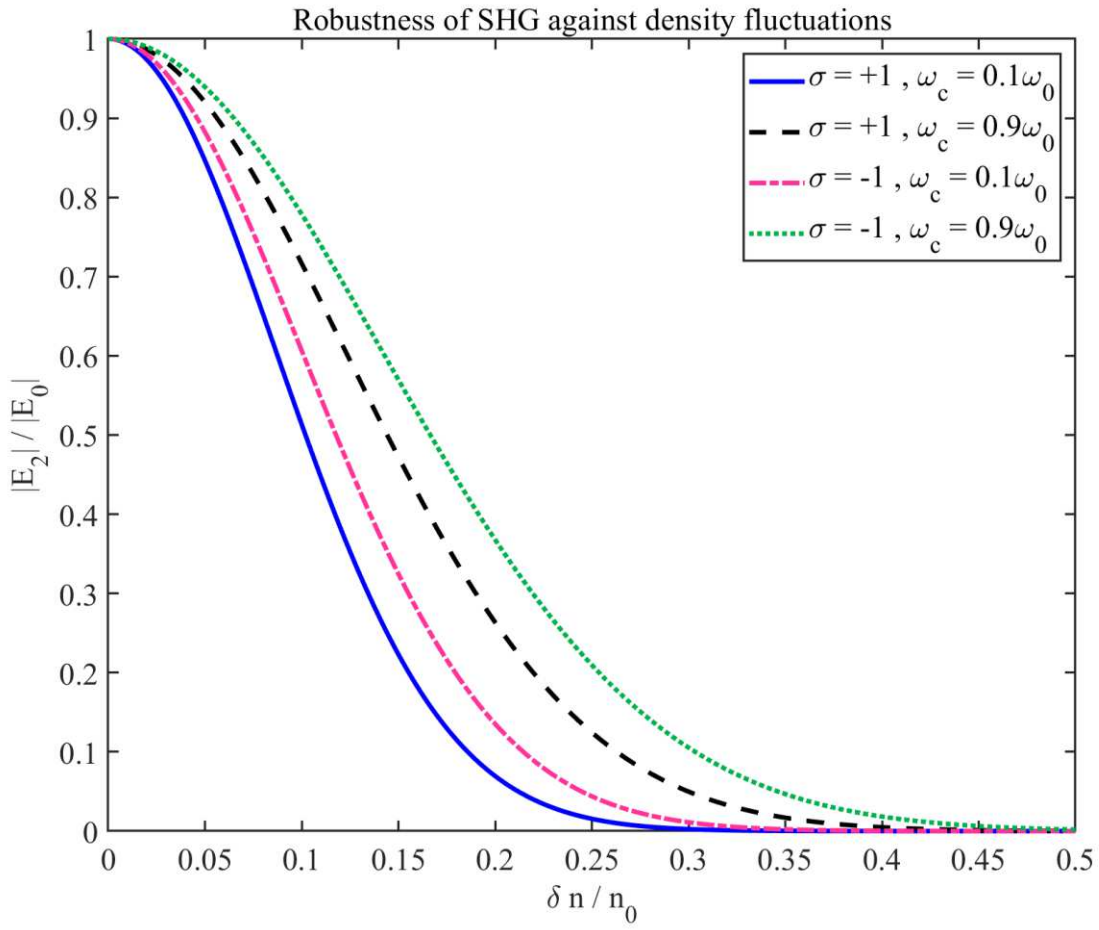

Robustness of SHG against density fluctuations
$\sigma = +1$, $\omega_c = 0.1\omega_0$
$\sigma = +1$, $\omega_c = 0.9\omega_0$
$\sigma = -1$, $\omega_c = 0.1\omega_0$
$\sigma = -1$, $\omega_c = 0.9\omega_0$
$|E_2| / |E_0|$
$\delta n / n_0$
0
0.1
0.2
0.3
0.4
0.5
0.6
0.7
0.8
0.9
1
0.05
0.15
0.25
0.35
0.45

Fig. 12.

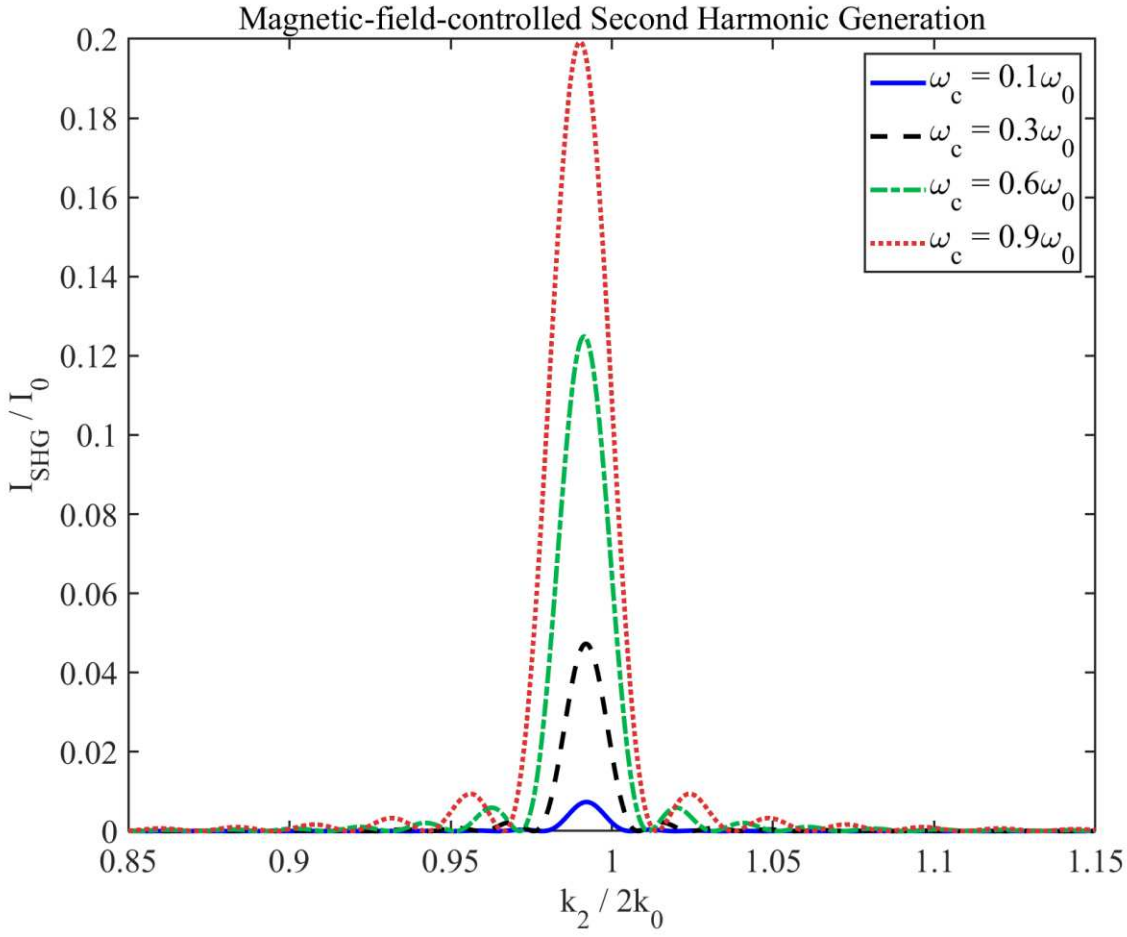

Magnetic-field-controlled Second Harmonic Generation
$\omega_c = 0.1\omega_0$
$\omega_c = 0.3\omega_0$
$\omega_c = 0.6\omega_0$
$\omega_c = 0.9\omega_0$
I_{SHG} / I_0
$k_2 / 2k_0$
0.2
0.18
0.16
0.14
0.12
0.1
0.08
0.06
0.04
0.02
0
0.85
0.9
0.95
1
1.05
1.1
1.15

Fig. 13.

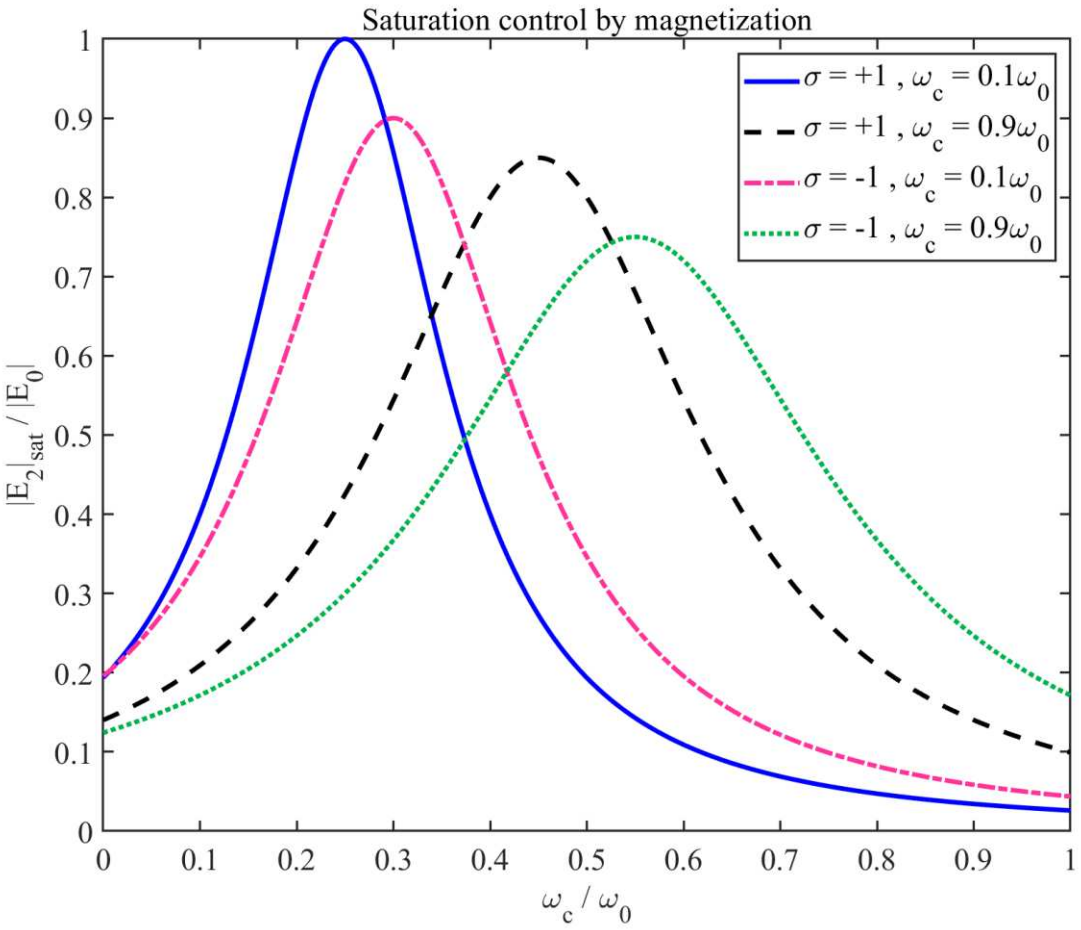

Saturation control by magnetization
$\sigma = +1$, $\omega_c = 0.1\omega_0$
$\sigma = +1$, $\omega_c = 0.9\omega_0$
$\sigma = -1$, $\omega_c = 0.1\omega_0$
$\sigma = -1$, $\omega_c = 0.9\omega_0$
$|E_2|_{sat} / |E_0|$
ω_c / ω_0
0
0.1
0.2
0.3
0.4
0.5
0.6
0.7
0.8
0.9
1

Fig. 14.